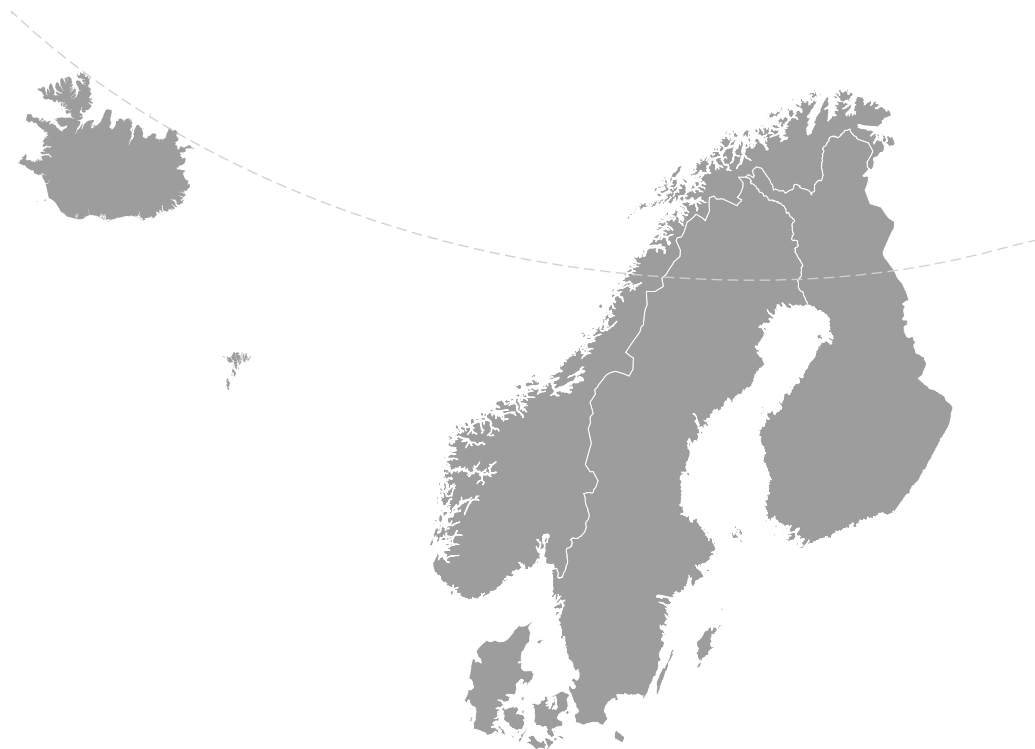


# Nordic Concrete Research



Nordic  
Concrete  
Federation



# **NORDIC CONCRETE RESEARCH**

**EDITED BY  
THE NORDIC CONCRETE FEDERATION**

**CONCRETE ASSOCIATIONS OF: DENMARK  
FINLAND  
ICELAND  
NORWAY  
SWEDEN**

**PUBLISHER: NORSK BETONGFORENING  
POSTBOKS 2312, SOLLI  
N - 0201 OSLO  
NORWAY**

**BREVIK/OSLO, DECEMBER 2016**



## Preface

*Nordic Concrete Research* is since 1982 the leading scientific journal concerning concrete research in the five Nordic countries, e.g., Denmark, Finland, Iceland, Norway and Sweden. The content of *Nordic Concrete Research* reflects the major trends in the concrete research.

*Nordic Concrete Research* is published by the Nordic Concrete Federation which also organizes the Nordic Concrete Research Symposia, a continuous series of conferences since its first onset in 1953 in Stockholm.

The next Nordic Concrete Research Symposium, no. XXIII, is organised in Aalborg, Denmark, on August 21. - 23. 2017. We do look forward to welcoming you there.

Since 1982, well over 400 papers have been published in the journal. Since 1994 the abstracts and from 1998 both the abstracts and the full papers can be found on the Nordic Concrete Federation's homepage: [www.nordicconcrete.net](http://www.nordicconcrete.net). The journal thus contributes to dissemination of Nordic concrete research, both within the Nordic countries and internationally. The abstracts and papers can be downloaded for free. In future, proceedings from miniseminars and the proceedings from the Research Symposia will also be published on the homepage.

The quality level of the papers in NCR is supervised by the group of reviewers. Most papers are assessed by two reviewers, selected according to their individual expertise.

Currently we are exploring the possibility to have NCR published by a larger international publisher, in order to increase the number of readers, and to have NCR accepted by international scientific databases. More information will be published on our homepage in due time.

Since 1975, in the range of 80 Nordic Miniseminars have been organized. It is the experience of the Research Council of the Nordic Concrete Federation, that these Miniseminars have a substantial influence on concrete research in the Nordic countries. In some cases, the information gathered during such Miniseminars has also been used as Nordic input to CEN activities. An overview is provided at our web page [www.nordicconcrete.net](http://www.nordicconcrete.net).

Brevik/Oslo, December 2016

Terje F. Rønning  
Temporary editor, *Nordic Concrete Research*



## CONTENTS

	Erratum of article in Volume 54	7
1	Esben Østergaard Hansen, Martin Riis Iskau, Marianne Tange Hasholt <b>Chloride ingress in concrete with different age at time of first chloride exposure</b>	9
2	Mahdi Kioumarsi, Esmahil Parsa, Mohammad Kazem Sharbatdar, Ali Kheyroddin, Gro Markeset <b>Ductility and structural characteristics of RC damaged frames strengthened with HPRCC layer</b>	27
3	Mahdi Kioumarsi, Mahdi Tajfar, Ali Kheyroddin, Benyamin Kioumarsi <b>Investigation of the seismic response of reinforced concrete column-beam connections using high performance fibre reinforced cementitious composites (HPRCC)</b>	36
4	Mohammed Mahal, Björn Täljsten, Thomas Blankswärd <b>Fatigue analyses of RC beams strengthened in flexure using CFRP</b>	49
5	Mattias Blomfors, Kamyab Zandi, Karin Lundgren <b>Development of engineering assessment method for anchorage in reinforced concrete</b>	63
	Research Council and Editorial Board of NCR	79



## ***Erratum of article in Vol. 54, June 2016***

### **Climate change effect on wind-driven rain on facades**

By Toni A. Pakkala, Antti-Matti Lemberg, Jukka Lahdensivu, Matti Pentti

- Section 4.3, third paragraph: Inclusion of definition: “ $\theta$  is a wall orientation relative to north [°]”
- Section 5, first paragraph: Inclusion of reference to equation 2 for the index ( $I_A$ )
- Figure 6 modified text: “Figure 6 – Relative amount of  $I_A$  compared to  $I_A$  from north direction at present climate from different wind directions at a) coastal area, b) southern Finland, c) inland and d) Lapland.
- Text paragraph under Figure 6, last sentence modification: “At the coastal area 74% of precipitation hits a vertical wall while at southern Finland the share is 66%, at inland 54% and at Lapland 53%.”
- Second text paragraph under Figure 7: Inclusion of reference to equation 1 for the index ( $I_{WA}$ )



## Chloride Ingress in Concrete with Different Age at Time of First Chloride Exposure



Esben Østergaard Hansen  
Master student (Civ. Eng), B.Sc.  
Technical University of Denmark  
Department of Civil Engineering  
Email: esbenhansen89@gmail.com



Martin Riis Iskau  
Master student (Civ. Eng), B.Sc. Eng.  
Technical University of Denmark  
Department of Civil Engineering  
Email: isriis@gmail.com



Marianne Tange Hasholt  
Associate professor, M.Sc., Ph.D.  
Technical University of Denmark  
Department of Civil Engineering  
Email: matah@byg.dtu.dk

### ABSTRACT

Concrete structures cast in spring have longer time to hydrate and are therefore denser and more resistant to chloride ingress when first subjected to deicing salts in winter than structures cast in autumn. Consequently, it is expected that a spring casting will have a longer service life.

This hypothesis is investigated in the present study by testing drilled cores from concrete cast in 2012 and 2013 on the Svendborgsund Bridge. The cores are subject to petrographic examination and mapping of chloride profiles. Moreover, chloride migration coefficients have been measured. The study shows that the effect of the extra time of hydration obtained when casting in spring increases the expected service life of the concrete structure significantly.

**Key words:** Chloride ingress, age-dependent chloride diffusion coefficient, field exposure, service life.

## 1. INTRODUCTION

Chloride ingress can lead to reinforcement corrosion, so for reinforced concrete structures exposed to seawater or deicing salts, the extent of chloride ingress often determines the structure's service life [1]. The resistance against chloride ingress mainly depends on four things: the constituents and mixing proportions of the concrete and the curing conditions and the age of the concrete, as the denseness of the concrete is developed over time [2].

Considering that the age plays a role in the transport properties of the concrete, it seems reasonable to assume that the age of the concrete at first exposure to chloride will play a role in the service life of the concrete. When concrete is relatively young, it will be more permeable, and therefore more chloride will enter into the concrete. Due to concentration differences, this chloride will keep moving into the concrete in the coming years, though the concrete at this stage has become more resistant to chloride transport.

It is the objective of this study to investigate the importance of the age at first chloride exposure for concrete that will be exposed to chloride throughout its service life. The study is conducted as a field study of chloride ingress on the Svendborgsund Bridge. The bridge underwent major repair in 2012 and 2013, and at the same time, the bridge got two new bike lanes. These are made of concrete without asphalt cover, so the concrete is directly exposed to de-icing salts during wintertime. The de-icing salt is the main source of chlorides. The chloride load from airborne chlorides is low due to the height of the bridge and the low salinity of the sea water. Both in 2012 and 2013, repair works started in spring and ended in autumn. Because of this, parts of the concrete were cast in spring and part of it in autumn, and as a result, there are concrete with very different ages at first exposure to chloride from de-icing salts. This offers a unique insight into the importance of concrete age at first chloride exposure.

### The Svendborgsund Bridge

The Svendborgsund Bridge was opened in 1966. It leads road traffic over Svendborg Sound, thereby connecting the two Danish islands Fyn and Tåsinge. The bridge is 1220 m long, and it has a ship passing height of 33 meters. On average, 16,000 cars pass the bridge every day [3].

## 2. THEORY

Concrete is a porous material, and concentration differences of ions will seek equilibrium by gradually diffusing through the pore solution. This includes chloride ions present at the surface of a concrete structure, e.g. as a result of deicing salt or because the structure is placed in marine environment. If the concentration of chloride ions in the concrete is too high, it can lead to corrosion of the reinforcement. The diffusion of chloride ions for a non-steady state situation in a saturated concrete can be described using Fick's 2<sup>nd</sup> law. The error-function solution to Fick's 2<sup>nd</sup> law can be used to calculate the chloride concentration to any point and at any time, see Equation (1).

$$C(x, t) = C_s - (C_s - C_i) \cdot \operatorname{erf}\left(\frac{x}{2\sqrt{D \cdot t}}\right), \quad (1)$$

Where

$C(x, t)$  concentration at depth  $x$  and time  $t$  [%],  
 $t$  time of exposure [s],  
 $x$  depth from free surface [m],  
 $C_s$  surface concentration [%],  
 $C_i$  initial concentration [%], and  
 $D$  diffusion coefficient  $\left[\frac{m^2}{s}\right]$ .

The design of the concrete recipe influences the diffusion coefficient significantly, as a denser concrete will yield a lower diffusion coefficient. The w/c ratio is one of the most influential parameters as a large w/c ratio leads to a more porous concrete. Earlier studies have shown that when the w/c ratio varies from 0.2 to 0.7 the diffusion coefficient varies with a factor of almost 50 [4]. The diffusion coefficient also decreases when the maturity increases, as concrete hardening is a continuous process making the concrete denser over time. According to Tang and Gulikers [5], the time dependency was first modeled by Takewake and Mastumoto [6] in 1988, and today there are a number of mathematical approaches to describe the time-dependent diffusion coefficient.

Apart from the parameters stated in Fick's 2<sup>nd</sup> law, other things may influence the chloride ingress. If the concrete is periodically dried out, the chloride ingress is not pure diffusion, as is the premise for Fick's 2<sup>nd</sup> law, as in this case also capillary suction can lead to chloride ingress. However, it seems generally accepted that the application of Fick's 2<sup>nd</sup> law is still useable to extrapolate the future chloride ingress and concentration [7, 8]. In other exposure situations than a pure diffusion situation, the measured diffusion coefficient is an apparent diffusion coefficient. In the following text, no distinction is made between "diffusion coefficient" and "apparent diffusion coefficient".

When determining the service life of a structure in relation to the chloride concentration in the concrete, a threshold must be set for the initiation of corrosion. An often-used value is 0.05% by weight of the concrete [9].

### 3. MATERIALS AND METHODS

#### 3.1 Materials

The concrete specimens are cores taken from the structure using vertical drilling on the bicycle tracks. The cores are taken at four locations, which are assumed to have the same chloride load (same rain intensity, same dosage of de-icing salts, same distance to car lane, etc.).

The concrete composition stated in the as-built documentation is specified in Table 1. The cement used is a cement in class CEM I 42.5 N. All aggregates fulfill the demands for Danish exposure class E (i.e. XD3/XS3 and XF4 according to EN 206). The coarse aggregates are granite. The water/binder ratio is 0.33. The concrete is air entrained, but the actual air void structure is not documented in the as-built documentation. It is assumed that the air void structure fulfilled the requirements for XF4 at time of erection (minimum air content in hardened concrete 3.5%, maximum spacing factor 0.20 mm).

*Table 1 - As built concrete recipe*

Composition	Density [kg/m <sup>3</sup> ]	Amount [kg/m <sup>3</sup> ]	Volume [l/m <sup>3</sup> ]
Cement	3200	420.0	131
Fly ash	2300	54.6	24
Water	1000	156.5	156
Air entrainment	1010	0.8	1
Plasticizer	1160	2.8	2
Super Plasticizer	1050	1.2	1
Sand 0-4mm	2630	563.2	214
Coarse aggregates 4-8mm	2680	164.8	62
Coarse aggregates 8-16mm	2680	384.6	144
Coarse aggregates 16-25mm	2680	549.4	205
Aimed air content 6% of volume	-	-	60
Total		2298	1000

In Table 2, it is specified at which age each core was first exposed to chloride, and for how long it has been exposed.

*Table 2 - Concrete specimen names, age at exposure, and total time of exposure*

Specimen ID	Casting date	Age at first exposure [days]	Total time of exposure* [days]
S12	24-05-2012	155	879
A12	08-10-2012	18	879
S13	10-04-2013	192	521
A13	03-09-2013	46	521

\* "Total time of exposure" is the time from first chloride exposure and until the core is drilled. It is assumed that chloride already in the concrete will ingress inwards in the concrete, also during periods, where the concrete surface is not exposed to chloride.

The same concrete cores are used for all tests. The tests are performed in the following order:

1. The cores are examined in the petrographic analysis (section 3.2)
2. The uneven bottom part of each cylinder is cut off and a 50 mm cylinder piece is cut of the bottom. This piece is used to measure the chloride migration coefficient (section 3.3).
3. Thin layers are grinded of the top part of the cylinder and used to measure the actual chloride ingress (section 3.4).

There are two cores from each location, i.e. a total of eight cores. All cores are subject to petrographic examination (1) and migration test (2). The chloride profile (3) is only registered for one core from each location, except for S12 where the chloride profile is registered for both cores to document the variation within a specific location.

### 3.2 Petrographic analysis

The drilled cores are subjected to petrographic analysis on macroscopic level to ensure that the chloride penetration measurements, as well as the migration coefficient measurements are performed on comparable concrete cores.

The purpose of the petrographic analysis is to determine the quality and condition of the drilled concrete cores as well as determine the differences between them. The petrographic analysis has been performed according to ASTM C856-14 [10] but limited to the following parameters:

- The dimensions of the drilled core, (diameter and height) are measured with a caliper.
- The maximum aggregate size is measured on the surface of the drilled cores with a caliper.
- A visual evaluation on the distribution of the larger aggregates is performed.
- An approximate coarse aggregate percentage evaluation is made. This is performed by placing a ruler along the drilled cores three places and noting for each centimetre mark whether it is pasta phase or aggregates. If a centimetre mark hits a reinforcement bar, the measurement point is excluded. The aggregate percentage is then calculated as the number of points noted in aggregates divided by the total number of measurement points.
- The cores are inspected for visible signs of alkali silica gel.
- A visual comparison of the colors of the pasta phase between the cores is made.
- A visual assessment of mixed in air as well as air entrapped during casting is made.
- Dimensions of the reinforcement are measured (if present in a core).
- Thickness of the concrete cover layer is measured (if reinforcement is present).
- A visual assessment of the fracture surface from when the core has been removed from the structure is made.
- A visual assessment of the texture of the top surface of the cores is performed.
- Additional observations are noted, including indications of the following: separation in the concrete, casting joints, honeycomb and cracks in the core or other features that could indicate poor quality concrete or casting.
- After the bottom part of the cores are cut off for chloride migration test (see section 3.3) the remaining parts of the test specimens are cut parallel to the drilling direction of the test specimens. A slice is cut with a thickness of about 1-2 cm using a diamond circular saw. The slice is cut from the edge of the test specimen to leave as much specimen for chloride profile test as possible (see section 3.4). It is evaluated whether the carbonation have occurred in any of the drilled cores, by checking for color change. If the concrete turns pink, when phenolphthalein is applied, no carbonation has occurred. If the concrete does not change color, when phenolphthalein is applied, carbonation has occurred.

The petrographic examination described above is performed on the intact cores. In addition, the carbonation depth is measured on saw cut slices of the cores, by spraying the slices with phenolphthalein.

### 3.3 Chloride migration coefficient

It is interesting to investigate whether the test specimens have comparable transport properties by determining their migration coefficients. Natural diffusion is a slow process, and it will take place while the diffusion coefficient is varying, so the diffusion coefficient derived from a

measured chloride profile from natural exposure does not represent the diffusion coefficient at the exact time of testing. Instead a migration test can be performed. This is a relatively quick test, as it only takes a few days to perform, and therefore it provides a better basis for comparing transport properties at a certain age.

In a migration test a section of the concrete core is exposed to one-directional transport of chloride under the influence of an external electrical field. The difference in electrical potential accelerates the diffusion of the Cl<sup>-</sup> ions. The test is created to estimate the migration coefficient as close as possible to the diffusion coefficient of saturated concrete at the same temperature. In the rest of the article, the diffusion coefficient determined by migration is denoted as migration coefficient.

In the present study, the chloride migration coefficient is performed according to NT BUILD 492 [11]. The purpose of the method is to determine a non-steady-state migration coefficient for chloride ingress in drilled concrete cores. The principle of the method is to force chloride through a section of a drilled concrete core by applying an electrical potential across the specimen. After a set period, the test specimen is split axially and a silver nitrate solution is applied to one of the split sections. In areas with chloride, white silver chloride precipitation is formed. The chloride penetration depth is measured as the distance from the surface exposed to chloride to the borderline, where the color changes. The measured penetration depth is then used to calculate the non-steady-state chloride migration coefficient.

### **3.4 Chloride ingress due to field exposure**

The rate of the chloride ingress as stated is depending on several parameters whereof the diffusion coefficient is the most predominant variable in specimens tested, as they are assumed to have experienced the same external conditions during exposure.

The method used in this study to produce a chloride profile closely resembles that of the standards NT BUILD 208 [12] and NT BUILD 443 [13] but instead of Volhard titration, a potentiometric titration is used, as this is the standard procedure at DTU Civil Engineering laboratory. To investigate how the distribution of the aggregates affects the chloride profile, a small sample is removed from each layer and the calcium content in the layer is determined via ICP (Inductively Coupled Plasma mass spectrometry). The chlorides can only penetrate the pasta phase which is the only component in the concrete that contains calcium. The chloride content of the concrete can be normalized in relation to the paste content in each layer.

The method is summarized in the following description:

- A drilled core is fixed in a grinding machine, exposed side up, making it possible to grind off thin layers of concrete dust at a time. Extra care is taken to make sure that the top surface of the core is level, so that the layers taken off are parallel with the exposed surface.
- The precise height of the core is noted using a digital caliper, to make it possible to determine the exact thickness of the layers ground off.
- A layer is ground off, and the dust produced is collected, the new height is noted.
- This process is repeated until it is estimated that chloride-ingress depth is reached.
- The sample is turned upside down, and a sample from the bottom is taken, to provide a sample for measuring the initial chloride concentration.

- The dust is chemically dissolved using nitric acid freeing the  $\text{Cl}^-$  ions.
- A small sample is removed for calcium analysis via ICP.
- 1 ml of 0.1 N NaCl solution is added to the sample for titration to ensure titration precision.
- The prepared sample is titrated using silver nitrate to find the chloride concentration.
- A chloride concentration profile is made from the measured depths and the amount of silver nitrate added.
- The exposure time is set to be the time between the concretes first exposure to frost, as this is likely the first time the road was exposed to deicing salts, and the time when the samples were collected. Data from the Danish Metrological institute's website was used to assess the first day of frost for each of the samples [14]. The chloride concentration from the bottom sample is used as the initial chloride concentration.
- The age of the test specimens at first exposure is shown in table 2.
- The chloride content for each layer is determined using the error function solution to Fick's 2<sup>nd</sup> law. The measuring point closest to the surface is excluded, as described in NT BUILD 443.

## 4. RESULTS

In this section all results from the experiments are presented along with the initial conditions for the experiments.

### 4.1 Petrographic analysis

In the following, the results from the different steps in the petrographic analysis are listed.

#### *Aggregates*

- The maximum observed aggregate in the cores, is between 16-27 mm in diameter.
- The aggregate can be considered evenly distributed.
- The coarse aggregate content measured in each specimen varies from 28-41% of the surface area, corresponding to an equal amount by volume, which only includes visible aggregates and therefore does not take small aggregates like sand into account. The prescribed coarse aggregate content is 47% by weight, and about 40% by volume, assuming an aggregate density of 2750  $\text{kg/m}^3$  for granite. The measured coarse aggregate content seems to correspond well to the prescribed volume.
- There are no visible signs of alkali-silica reactions. Furthermore, the coarse aggregates seem to be granite based.

#### *Paste*

It is assessed that the colors of pasta phase are comparable and no soft spots are found on the surface of any of the drilled cores.

#### *Air void structure*

The concrete is air-entrained, and the air voids are well distributed. There are a few entrapments of air.

### Reinforcement

The assessed dimension of the reinforcement bars found in the cores are 12 and 17 mm. Reinforcement are not usually sold in 17 mm why it is assessed that the full diameter is larger than 17 mm, possibly 20 mm. The concrete cover layer is registered to 55 mm for the 17 mm reinforcement bars and 75mm for the 12mm reinforcement bars.

### Carbonation

Phenolphthalein solution was applied to make the carbonation front visible. The carbonation depth was in all cases lower than 1 mm.

### Additional observations

- The fractured surfaces in the bottom of the drilled cores are similar with fracture occurring both through aggregates and pasta phase, which indicates that the pasta phase have a high strength.
- On several cores a different concrete type are observed in the bottom of the core, indicating that the bike lanes are casted on top of an existing structure. The condition of the concrete of the existing structure has not been evaluated.

From this, it can be concluded that all of the concrete samples are sound and meet the specifications for the concrete, and they therefore appear to be comparable.

## 4.2 Chloride migration coefficient

The results of the chloride migration test are presented in Figure 1.

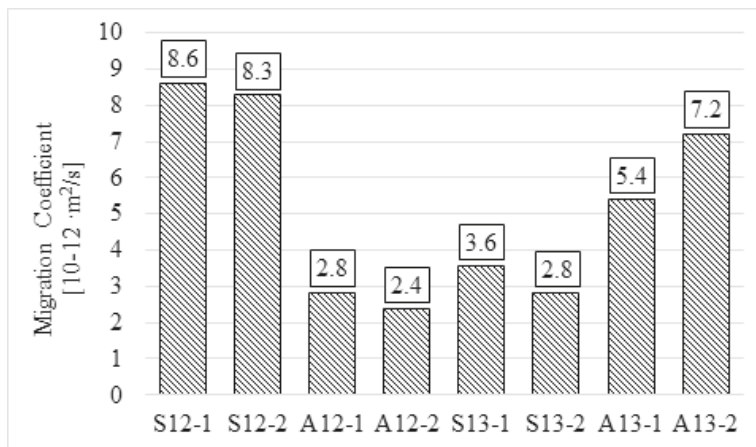


Figure 1 – Migration coefficients

### 4.3. Chloride ingress due to field exposure

Of the eight drilled cores studied in this paper, a chloride profile analysis is made for five of them, one from each set of cores and both from one set, to document the variation within a specific location. The results can be seen in Figure 2. An average of the initial concentrations, found from analysing the bottom of the sample, is plotted along the bottom of the graph.

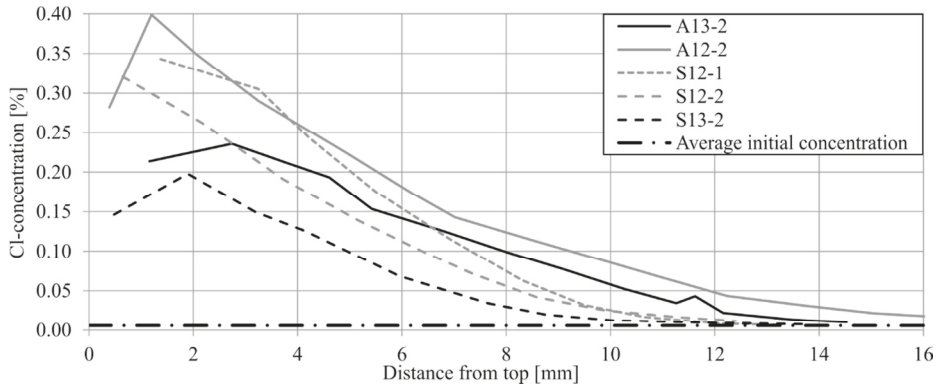


Figure 2 - Comparison of the different chloride ingress profiles

Using the error function solution for Fick's 2<sup>nd</sup> law, the diffusion coefficient  $D$  and the surface concentration  $C_s$  are found for each sample. The measuring point closest to the surface is not used in the curve fit. This is according to practice in [13]. For most of the profiles, the chloride concentration measured closest to the surface is lower than the concentration measured in the second closest point. This is not physically meaningful according to Equation (1).  $C_i$  is set to be equal to the concentration found in the bottom of the sample. The error function solution is plotted as a curve next to the measured data in Figure 3.

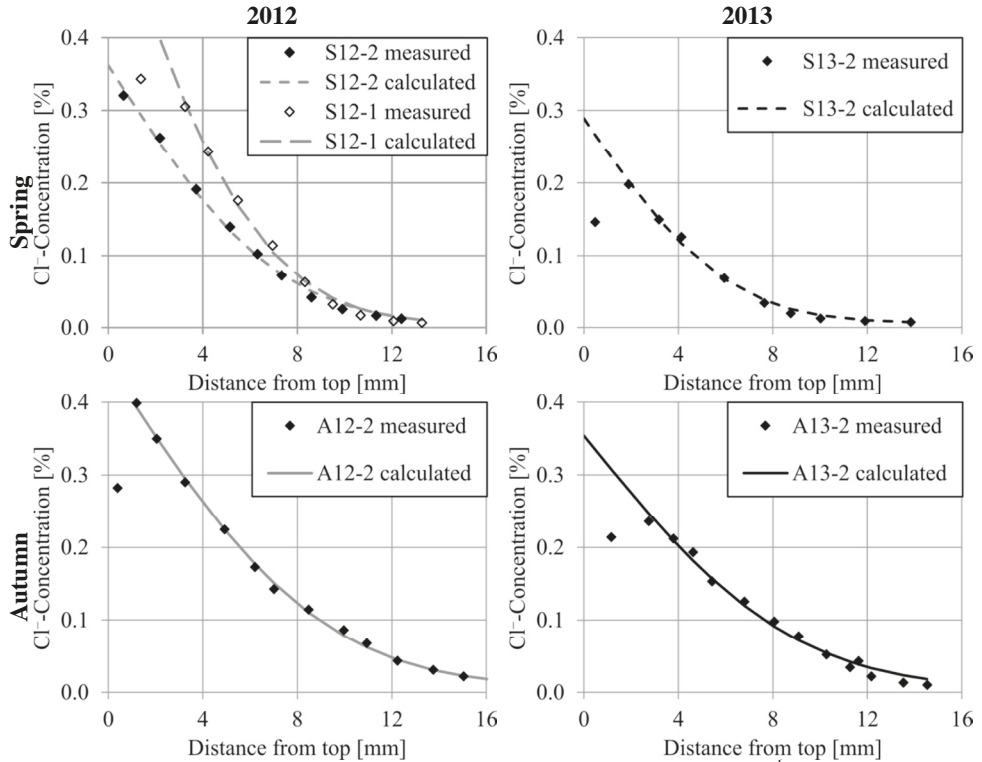


Figure 3 - Measured compared to calculated concentrations using Fick's 2<sup>nd</sup> law

The concentrations in the points closest to the surface can be misleading, so even though all of the data is displayed, only the point matching a diffusion curve with decreasing concentrations as the distance to the surface increases are used to determine the diffusion coefficient by curve fitting.

As mentioned earlier a sample was taken from each layer to measure the calcium concentration. The results of this can be seen on Figure 4.

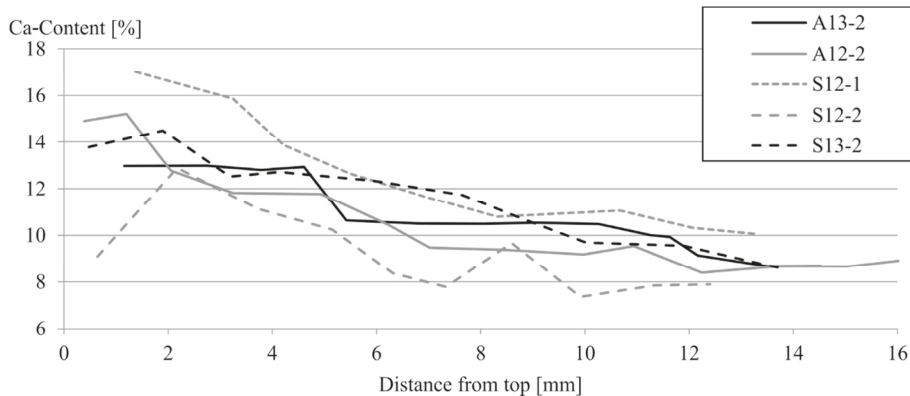


Figure 4 - Ca-concentrations

The concentration is higher in the surface layer of the sample due to uneven distribution of cement paste. The calcium concentration evens out at depth 10-12 mm, corresponding to approximately half the maximum aggregate size. The calcium concentration profiles can be used to correct errors in the chloride profile.

## 5. DISCUSSION

### 5.1 Petrographic examination

Based on the observations made during the petrographic analysis of the drilled cores it is concluded that the execution of the concrete works are of high quality and consistent. The amount of entrapped air is larger in the castings performed in 2013 compared to the castings made in 2012. However, the amount of air entrapments along with the distribution is assessed not to influence the quality of the final durability of the concrete significantly. The concrete is air entrained and there are no signs of damage that can be related to frost action. The carbonation is hardly noticeable in the drilled concrete cores.

### 5.2 Chloride migration coefficient

The results in Figure 1 show that the migration coefficients for samples from the same location are on the same level. According to the test method [11], the coefficient of variation of repeatability is 9%. For some of the locations, the difference between two measurements surpasses 9%, but that is because the specimens are not fully identical.

Migration coefficients between different locations vary. The largest migration coefficient is 3.6 times larger than the smallest migration coefficient. This is a significant difference, as the difference is much larger than the accuracy of the test method. There does not seem to be a systematic trend as regards casting season; for samples cast in 2012 the migration coefficient for the spring casting is higher than the migration coefficient for the autumn casting, but in 2013 the results show the opposite. There is no systematic trend as regards the age of the sample either. The highest migration coefficient is registered for the oldest sample, and this was expected to have the lowest migration coefficient. However, the migration coefficient is highly dependent

on the mix composition. In a concrete production (not a laboratory mix) it is likely that the w/c ratio varies up to  $\pm 0.02$  from the target w/c ratio of the recipe, and this can explain the differences in migration coefficients.

Moreover, local variations may lead to some uncertainty of the results. Figure 5 shows the split samples from the migration test for two samples from the same location.

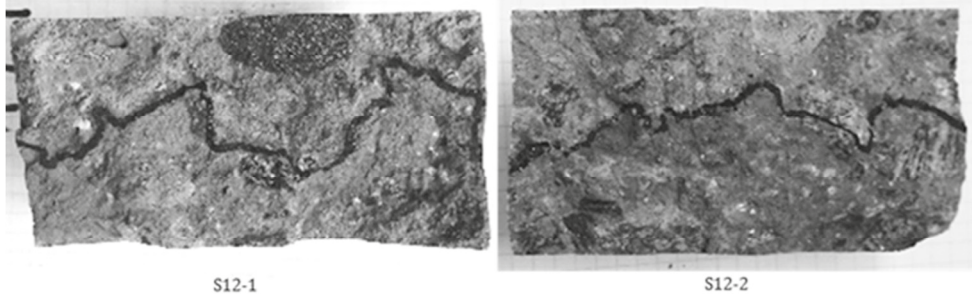


Figure 5 - Chloride migration profiles from accelerated migration coefficient test. The pictures are color adjusted for better contrast

It is observed that even though the migration front of the two samples shown in Figure 5 should be similar, as they are paired samples, it varies a lot. In S12-1 it looks like the chloride have penetrated the specimen much deeper at the dark aggregate that shows up in the figure. This may indicate that the aggregate may have been porous and have accelerated the chloride transport through the aggregate itself. A closer examination of the aggregate indicates that it is not granite like the rest of the aggregates; however a final conclusion on the influence of the aggregate could not be made.

### 5.3 Chloride ingress due to field exposure

Figure 4 shows that the calcium content (and therefore also the paste content) is highest closest to the surface. The calcium content seems to reach a stable value 10-12 mm from the surface. This equals approximately half of the maximum aggregate size, which is 25 mm.

As mentioned, the chloride concentrations can be corrected with the use of the calcium concentrations. Figure 6 shows the same data as Figure 3, but now the chloride content is normalized to the calcium content. It can be observed that the difference between cores from the same location S12-1 and S12-2 seen in Figure 3 has now disappeared, so the explanation for the difference seems to be differences in paste content. The point closest to the surface still has a lower concentration than the second point. This may be related to the exposure situation, e.g. that chloride in the very surface layer is washed out by rain in the spring.

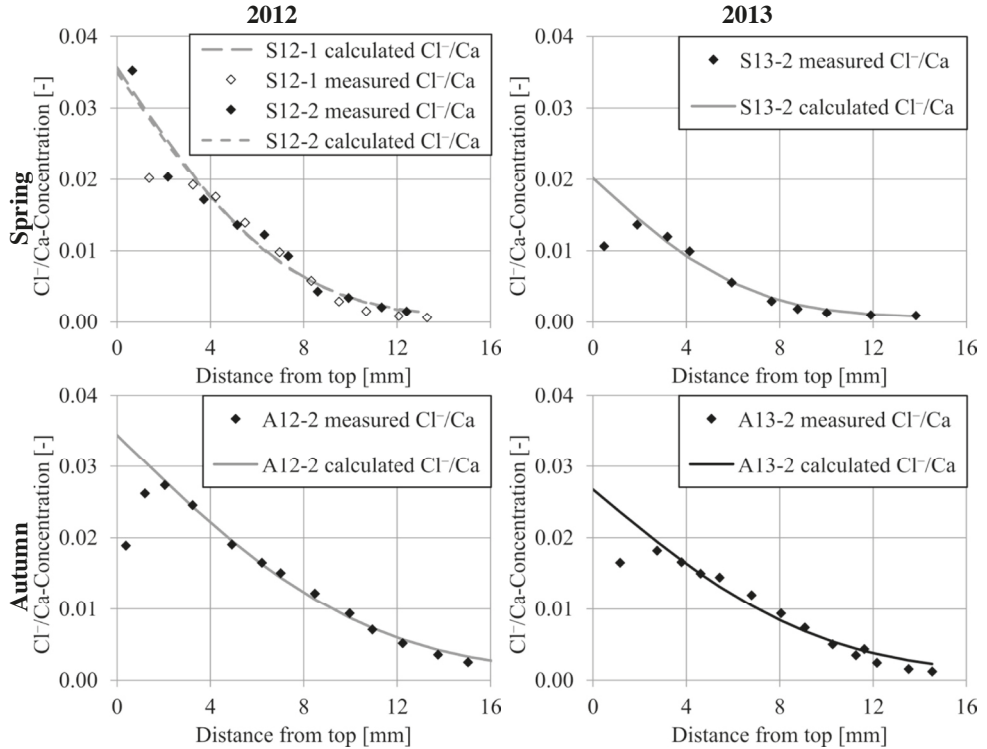


Figure 6 - Measured concentrations compared to concentrations calculated using Fick's 2nd law. Ca-calibrated.

From the calculated profiles shown in Figure 6, the surface concentrations and the diffusion coefficients can be found for Ca-calibrated measurements, as it was done for the un-calibrated measurements in Figure 3. The diffusion coefficients found for the un-calibrated and calibrated measurements are compared in Figure 7. The general trend is that the diffusion coefficient found for Ca-calibrated measurements is higher than the diffusion coefficient found by curve fitting to un-calibrated measurements. This is to be expected, when the paste content is higher near the surface than the average paste content of the bulk concrete. The largest difference is found for A12-2, where the diffusion coefficient is increased 42% by the calcium calibration.

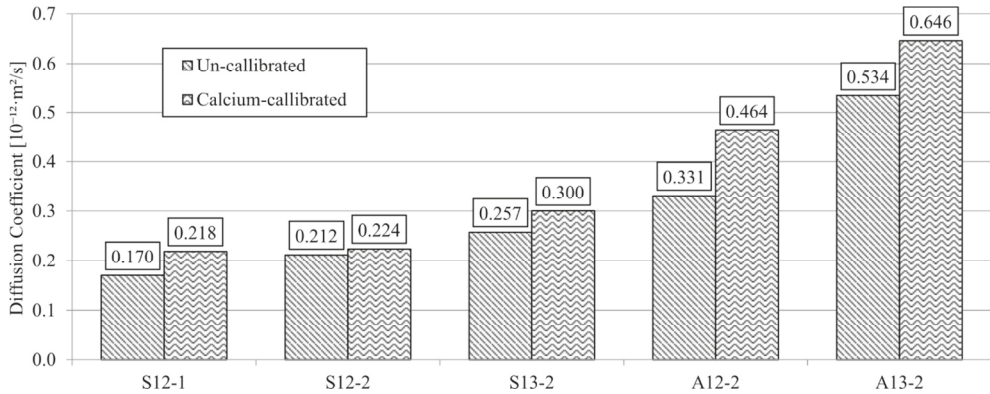


Figure 7 - Comparison of diffusion coefficients.

The calcium-calibration does not change the picture that can be observed in both Figure 3 and Figure 6. In both figures it is observed that the chloride ingress is lower in the cores cast in spring than the ones cast in autumn. Figure 7 shows that the diffusion coefficients are notably higher for the autumn castings than for the spring castings. This conflicts with the results of the migration test. The migration test results show no clear tendency that the autumn cores have a higher diffusion coefficient than the spring cores. If the migration coefficients had shown the same tendency, the results could be contributed to the concrete quality, different curing conditions, etc. Now, the most likely explanation seems to be the chloride ingress at early age in the samples from autumn castings. As stated earlier, the migration coefficient measurement is made over a very short time, where the diffusion coefficient is expected to be constant within the test period. The diffusion coefficient calculated using the chloride ingress profile is a sort of weighted average for the time where the concrete has been exposed to chlorides. Here it can change the result, if the exposure period comprises a period, where the concrete was young and therefore had a high diffusion coefficient.

Furthermore, Figures 3 and 6 show that cores from 2012 have a higher chloride surface concentration than the cores cast in 2013. On one hand, this may be because the surface concentration is gradually building up, and the cores from 2012 have been exposed to three winter seasons compared to the cores from 2013, which have only been exposed to two. On the other hand, it may be because the surface concentration was essentially established in the first winter season, and the winter 2012/2013 gave rise to more heavily use of de-icing salts than the following two winter seasons. It is not possible to determine which of the two explanations that is correct, and it is also possible that they both play a part.

#### 5.4 Effect of casting season on service life

When the ingress parameters  $C_s$ ,  $C_i$ , and  $D$  are known, it is in principle possible to predict when the chloride concentration at the reinforcement level reaches a critical level and thereby assess the potential service life. The obtained diffusion coefficients are based on the chloride ingress that have taken place in the first years of the life of the structure, and extrapolation from these data are normally conservative, as the diffusion coefficient will continue to decrease with developing maturity.

The present data shows the difficulties in making a precise service life prediction. It is probably the measured migration coefficients that are best in ranking the transport properties anno 2015 of the concrete castings, i.e. in which casting the chloride transport is fastest and slowest. But the measured migration coefficients cannot be used for prediction of service life, as the test circumstances do not represent the actual exposure conditions. The migration coefficients are at least a factor of ten higher than the diffusion coefficients deduced from the chloride profiles.

If the chloride profiles are extrapolated in time to predict the service life, then the diffusion coefficients of the autumn castings are approximately twice the value of the diffusion coefficients of the spring castings. According to Equation (1), the time needed to reach a certain concentration at reinforcement level will be twice as long for a spring casting, compared to an autumn casting. However, this will overestimate the effect of the casting season, as the factor 2 between diffusion coefficients is not a realistic representation of difference in the transport properties in the long run. There will also be significant differences between the predicted service life based on measurements from castings in 2012 and 2013, due to differences in surface concentrations, i.e. predictions based on measurements for castings in 2013 will result in longer service lives, due to lower surface concentrations. The surface concentrations are expected to become more equal over the years, as the effect of the first winter season exposure will vanish.

Despite the challenges in predicting the service life accurately, it is possible to estimate the effect of the casting season by using the analogy of equivalent cover layer thickness, which can also be used to evaluate the effect of surface coatings [15]. Four test specimens exist, cast in in respectively spring and autumn of two consecutive years. It is assumed that the chloride exposure are identical for each test specimen location within each year, and so two chloride exposure histories exist, one for each year.

The principle is to calculate the difference in the initial chloride ingress by translating the spring data horizontally in the plots in order to calculate the extra cover layer needed to obtain the same service life for an autumn casting as for a spring casting. The calculation is made by including the extra depth needed to fit the chloride profile of the spring test specimens to that of the autumn ones in the solving process along with the surface chloride concentration and the diffusion coefficient.

The fitted results are presented in Figure 8.

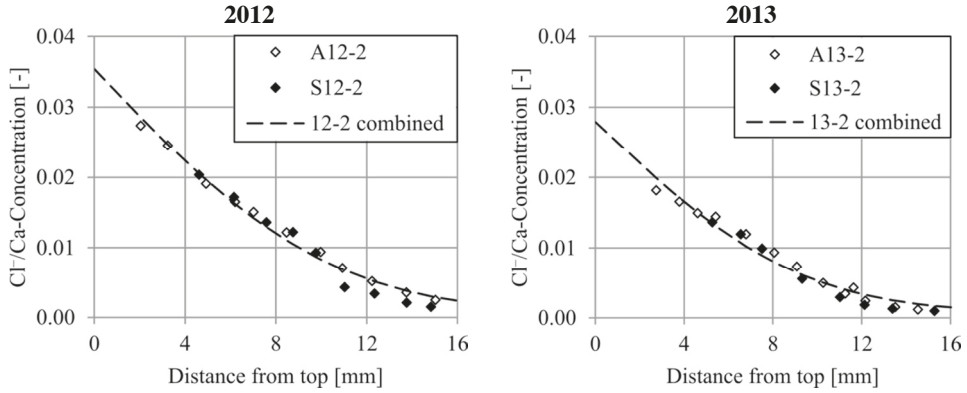


Figure 8 – Calculation for assessment of extra cover layer.

The castings performed in 2012 and 2013 result in differences in concrete cover layer of 2.4 mm and 3.4 mm, respectively.

If the imaginary reduction of the cover layer of the autumn casting is denoted  $\Delta x$ , then the service life of an autumn casting relative to a spring casting can be calculated by rearranging Equation (1) and assuming that the critical chloride concentration will be the same in the two cases, see Equation (2):

$$\begin{aligned}
 C(x, t) &= C_s - (C_s - C_i) \cdot \operatorname{erf}\left(\frac{x_{\text{cover}}}{2 \cdot \sqrt{D \cdot t_{\text{spring}}}}\right) = C_s - (C_s - C_i) \cdot \operatorname{erf}\left(\frac{x_{\text{cover}} - \Delta x}{2 \cdot \sqrt{D \cdot t_{\text{autumn}}}}\right); \quad (2) \\
 \Rightarrow \frac{x_{\text{cover}}}{2 \cdot \sqrt{D \cdot t_{\text{spring}}}} &= \frac{x_{\text{cover}} - \Delta x}{2 \cdot \sqrt{D \cdot t_{\text{autumn}}}}; \\
 \Rightarrow t_{\text{autumn}} &= t_{\text{spring}} \cdot \left(\frac{x_{\text{cover}} - \Delta x}{x_{\text{cover}}}\right)^2.
 \end{aligned}$$

Where

- $x_{\text{cover}}$  cover layer thickness [m],
- $t_{\text{spring}}$  service life for a spring casting, and
- $t_{\text{autumn}}$  service life for an autumn casting.

In Table 3, the reduction in service life for an autumn casting is calculated for two different cover layer thicknesses; 40 mm, which is the minimum allowable cover layer in extra aggressive environment in Denmark [16] and 55 mm, which was the minimum cover layer registered in the cores from Svendborgsund Bridge.

Table 3 – Reduction in service life for an autumn casting, given different assumptions

	Cover layer		
		40 mm	55 mm
Cover layer	2.4 mm (2012)	12 %	9 %
reduction $\Delta x$	3.4 mm (2013)	16 %	12 %

As can be seen in Equation (2), the calculation in reduction of service life is independent of the assumed critical chloride concentration. The calculation can also be performed, without estimating the service life for a spring and autumn casting, respectively.

## 6. CONCLUSION

It is concluded, based on the chloride ingress measurements from the field exposed test specimens, that the age at which concrete is subjected to chloride for the first time has a significant influence on the chloride ingress in the structure. When concrete is exposed to chlorides at an early age the resulting higher diffusion coefficient of the concrete will result in deeper and faster chloride ingress in the structure. This results in earlier initiation of corrosion of the steel reinforcement, and therefore a shorter service life. How much the service life is reduced, depends on the total cover layer thickness. For the field exposed cores investigated in this study, where the cover layer is 55 mm, the expected service life is calculated to be 9-12 % shorter when the concrete is cast in the autumn compared to when the concrete is cast in the spring. If the cover layer had been only 40 mm, the reduction in service life would be 12-16 %. This knowledge should be taken into account when planning future concrete structures with risk of chloride exposure.

## ACKNOWLEDGEMENT

The Svendborgsund Bridge is administered by the Danish Road Directorate. We appreciate the co-operation with and support from the Road Directorate during the project. The Road Directorate gave access to documentation, e.g. drawings and mix design specifications, from their archive. Moreover, the Road Directorate provided the samples for the laboratory testing, as concrete cores were taken in connection with other works on the Svendborgsund Bridge.

## REFERENCES

- [1] Bertolini, L.: Steel corrosion and service life of reinforced concrete structures, *Structure and Infrastructure Engineering*, vol. 4, no. 2, pp. 123-137 (2008).
- [2] Chloride resistance of concrete, report, Cement Concrete & Aggregates Australia (2009).
- [3] Webpage of the Danish Road Directorate:  
[http://vejdirektoratet.dk/DA/viden\\_og\\_data/statistik/trafikken%20i%20tal/hvor\\_meget\\_trafik\\_er\\_der\\_paa\\_vejen/Trafikstrømskort/Documents/2013%20aadt/Kort12.pdf](http://vejdirektoratet.dk/DA/viden_og_data/statistik/trafikken%20i%20tal/hvor_meget_trafik_er_der_paa_vejen/Trafikstrømskort/Documents/2013%20aadt/Kort12.pdf)  
 (downloaded 2015-09-17).
- [4] Jensen, O. M., Hansen, P. F., Coats, A. M., & Glasser, F. P. (1999). Chloride ingress in cement paste and mortar. *Cement and Concrete Research*, 29, 1497-1504.
- [5] Tang, L., Gulikers (2007). On the mathematics of time-dependent apparent chloride diffusion coefficient in concrete, *Cement and Concrete Research*, 37, 589-595.
- [6] Takewaka, K., Mastumoto, S. (1988). Quality and cover thickness of concrete based on the estimation of chloride penetration in marine environments, in proceedings: V. M. Malhotra (ed.), 2<sup>nd</sup> Int. Conf. Concr. Marine Envir., ACI SP-109, 381-400.
- [7] Bentz, D. P., Guthrie, W. S., & Jones, S, Z, (2014). *Predicting Service Life of Steel-Reinforced Concrete Exposed to Chlorides*. Gaithersburg: Department of Civil and Environmental Engineering, Brigham Young University.

- [8] Tang, L., Lindvall, A. (2013). *Validation of models for prediction of chloride ingress in concrete exposed in de-icing salt road environment*. Gothenburg: Department of Civil and Environmental Engineering, Chalmers University of Technology.
- [9] Bertolini, L., Elsener, B., Pedersen, P., Redaelli, E., & Polder, R. (2013). *Corrosion of Steel in Concrete: Prevention, Diagnosis, Repair, Second Edition*. Wiley-VCH Verlag GmbH & Co. KGaA.
- [10] ASTM International. (2014). *ASTM C856-14, Standard Practice for Petrographic Examination of Hardened Concrete*. West Conshohocken, PA: ASTM.
- [11] Nordtest. (1999). NT BUILD 492 - Concrete, mortar and cement-based repair materials: Chloride migration coefficient from non-steady-state migration experiments. Nordtest, Espoo, Finland.
- [12] Nordtest. (1996). NT BUILD 208 - Concrete, hardened: Chloride content by Volhard titration. Nordtest, Espoo, Finland.
- [13] Nordtest. (1995). NT BUILD 443 - Concrete, hardened: Accelerated chloride penetration. Nordtest, Espoo, Finland.
- [14] Webpage of the Danish Meteorological Institute:  
<http://www.dmi.dk/vejr/arkiver/vejrarkiv/>  
(downloaded 2015-06-15)
- [15] Nordtest. (1999). NT BUILD 489 – concrete, hardened, repair: Chloride penetration resistance of paint on concrete. Nordtest, Espoo, Finland.
- [16] Danish Energy Agency. (2011). DS/EN 1992-1-1 DK NA:2011, Nationalt annekst til Eurocode 2: Betonkonstruktioner – Del 1-1: Generelle regler samt regler for bygningskonstruktioner (in Danish).

## Ductility and structural characteristics of damaged RC frames strengthened with HPFRCC layer



Mahdi Kioumars  
Associate Professor  
HiOA, Department of Civil Engineering and Energy Technology  
PI 830, Pilestredet 35, Oslo  
E-mail: mahdi.kioumars@hioa.no



Esmahil Parsa  
M.Sc, Structural Engineer  
Semnan University, Department of Civil Engineering  
E-mail: parsainfo173@gmail.com



Mohammad Kazem Sharbatdar  
Associate Professor  
Semnan University, Department of Civil Engineering  
E-mail: msharbatdar@semnan.ac.ir



Ali Kheyroddin  
Professor  
Semnan University, Department of Civil Engineering  
E-mail: [kheyroddin@semnan.ac.ir](mailto:kheyroddin@semnan.ac.ir)



Gro Markeset  
Professor  
HiOA, Department of Civil Engineering and Energy Technology  
PI 830, Pilestredet 35, Oslo  
E-mail: [gro.markeset@hioa.no](mailto:gro.markeset@hioa.no)

### ABSTRACT

In this paper, experimental strengthening of damaged frame with high-performance fibre-reinforced cementitious composites (HPFRCC) under lateral and gravity loads is investigated. Reference frame was tested up to its ultimate load capacity, then another frame was tested up to 75 % of its ultimate capacity and while remaining as damaged, strengthening with HPFRCC layer was done at the critical lengths. The strengthening was shown to improve the ductility of the frame up to 168 % as compared to the reference frame. The ultimate load of the frame was shown to increase significantly.

**Key words:** High-performance fibre-reinforced cementitious composites, strengthened, concrete frame, ductility, yielding load.

## 1. INTRODUCTION

In general, concrete is the most extensively used construction material worldwide. The application of concrete as a high quality construction material in structures exposed to severe loading conditions was introduced by the development and production of high strength concrete (HSC)/high performance concrete (HPC). Since mid-seventies, there has been a huge increase in the use of such HSC/HPC in offshore and bridge construction in Norway and elsewhere. However, the increased compressive strength obtained by reducing the water-cement ratio to 0.40 (or somewhat lower), leads to a more brittle material behaviour compared to normal strength concrete [1, 2]. For concrete structures exposed to severe dynamic loadings, like impact and earthquake, ductile structural response is of importance. By adding steel fibres to the concrete mix of HSC, the tensile properties could be increased substantially [3]. Compared to HSC without fibres, steel fibre reinforced HSC may substantially increase both shear capacity and impact resistance as well as the ductility of reinforced concrete (RC) slabs exposed to impact loadings [4, 5].

One application of high performance concrete is retrofitting damaged RC structures. Recently, employment of high-performance fibre-reinforced cementitious composites (HPFRCC) has been proposed for retrofitting of concrete structures [6-11]. HPFRCC can be classified as a high-strength material, depending on the stress-strain characteristic of the composite included. If the stress-strain diagram indicates strain hardening after initial cracking, then the composite is classified as a high-strength material. Otherwise, the material is termed an ordinary fibre-reinforced composite (FRC) the stress-strain diagram of which exhibits strain softening immediately after initial cracking. Therefore, HPFRCC is a special type of FRC which, under tension exhibits strain hardening after initial cracking, accompanied by multiple cracks before relatively high strains are developed [12].

Two types of HPFRCC have been developed: Ductal® composites and engineering cementitious composites (ECC). The former is the result of research conducted in 1981 [13]. A stiff dense mortar as well as high-strength fibres is used to produce this type of composite. A strong bond is created between the fibres and the mortar due to the high strength of the mortar, leading to high material strength after cracking. By using high strength fibres, this type of composite can be designed for elastic applications where fibres play a significant role under extreme conditions by tolerating tensile loads. According to the research conducted in 2003 [14], the tensile strength and ductility of this composite are 12 MPa and 0.02-0.06 percent, respectively.

The ECC are designed as both elastic and plastic materials. The fibres embedded in these materials enable them to effectively behave under serviceability and ultimate limit conditions. Li (1993) and Fisher (2003) studied ECC and reported a tensile strength of 4-6 MPa and ductility of 3-5 % for it [15, 16]. Compressive strength of high-performance fibre-reinforced cementitious composites (HPFRCC) indicates no significant difference in comparison with mass concrete or high strength concrete and is usually ranging from 20 to 90 MPa. After formation of the first crack, stiffness of reinforced concrete with HPFRCC becomes equal to or higher than normal concrete, this is attributable to the fact that cement composites reinforced with high performance fibres are able to share the load with steel reinforcement [17]. In an experimental research conducted by Hemmati, concrete

beams with layers of HPFRCC, built with same geometric dimensions and rebar configuration, were used and all specimens were tested in two pint loading. According to the results, the highest ductility was gained in a beam made fully of HPFRCC materials. This is attributable to the fact that the compressive and tensile strains of concrete specimen with HPFRCC layer is higher than specimen with normal concrete [18, 19]. Fischer and Li [20] studied effect of matrix ductile matrix on the response of steel reinforced flexural member under lateral load. Recent research has indicated a better strain hardening behaviour of HPFRCC concrete in comparison with normal concrete. The behaviour of beams, made of ductile materials and connected in coupled shear walls, has been evaluated by Parra [21-22].

As indicated by the introduction, HPFRCC is an appropriate substitute material for strengthening RC connection, originally containing ordinary concrete. This paper reports experiments made for strengthening a damaged reinforced concrete frame with HPFRCC layer in its critical zones. Testing of the strengthened frame was done using lateral and gravity loads. Material properties of the tested specimens and main results of the tests are presented in sections to follow.

## 2. PROPERTIES OF TEST SPECIMENS

### 2.1. Grading of the concrete mixes

The grading properties for the ordinary and HPFRCC concretes are shown in Table 1. The coarse aggregate used in the concrete consists of grain sizes of 0.51 inches (12.5 mm) to 4 inches (4.75 mm) with sands smaller than 4.75 inches (12.5 mm). The type of cement used was Portland, type 2. For strengthening of the concrete, polypropylene fibres (Makro sentetic), PPS, with 1 % relatives to the volume of concrete were employed. To avoid of reducing the water-cement ratio of the mix, plasticizers were added.

*Table 1 – Grading of concretes for the frames*

Concrete	Gravel	Sand	Cement	Water	w/c	Steel fibre	Micro silica
Ordinary concrete	834	1111	295	199	0.61	-	-
HPFRCC with PPS fibres	—	1730	470	199	0.38	9	23.5

### 2.2. Details of tested frames

In this study, three RC frames were built with similar geometries. Arrangement of reinforcements and geometry details of frames are shown in Figure 1. The yielding stress of longitudinal reinforcement and stirrups is equal to 420 MPa. Diameters of longitudinal rebars for beams and columns are 10 mm and 12 mm, respectively. Stirrups of 6 mm size are spaced at 100 mm both in beams and columns. The nominal size of the frames is 1 × 1.6 m, with the columns connected to a foundation that is assumed rigid.

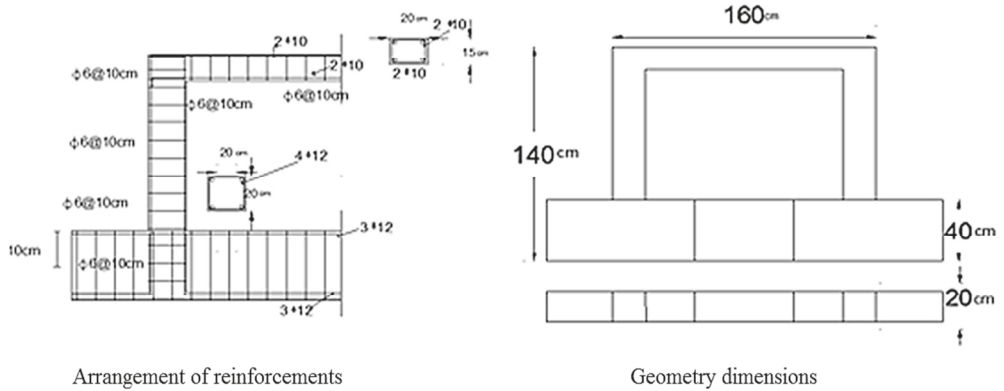


Figure 1 – Arrangement of reinforcements and geometry details of experimented frames.

### 2.3. Testing programme

The frame used as the reference structure (RCF) was built first and tested under a constant vertical load of 150 kN and an increasing lateral load for determining the ultimate load and detecting the general behaviour. Another frame, denoted as RCFE, was used to create a damaged specimen by loading it up to 75 % of the maximum capacity of the RCF.

For investigating the effect of strengthening and repair, the RCFE frame was then treated with HPFRCC and PPS fibres. The frame so produced is named RCJF75. The strengthening was done in the panel zone and within the plastic hinges at lengths equal to twice the depth of the beam and twice the depth of the column cross-section. Definition and details of the frames are presented in Table 2. Figures 2 and 3 show the reference and strengthened frames prior to testing.

Table 2 – Definition of abbreviation of experimental tested frames

No.	Name	Description
1	RCF	Reference concrete frame, loaded to ultimate state of collapse
2	RCFE	Frame damaged by loading it to 75 % of the ultimate load of the reference frame
3	RCJF75	The RCFE frame strengthened with HPFRCC and PPS

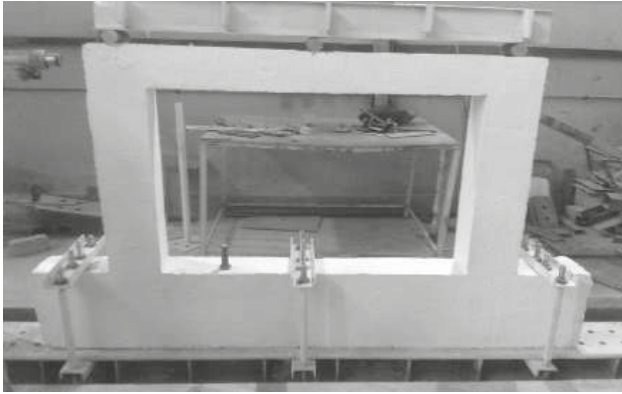


*Figure 2 – Reference frame (RCF) before testing.*



*Figure 3 – Initially damaged frame strengthened with HPFRCC (RCJF75) before testing.*

### **3. TEST RESULTS**

The cylinder strength of the conventional concrete at the time of testing of the frame was 38.82 MPa and the respective strength of HPFRCC concrete at the age of 7d was 37.5 MPa. Compressive strength (cylinder specimen) of conventional concrete during testing frames (almost three months after casting concrete) and HPFRCC concrete with one-week age were 38.82 and 37.5 MPa, respectively.

Figure 4 shows the load-displacement curves of the reference frame (RCF) and the initially damaged frame (RCFE). The load-displacement curves of the reference frame (RCF) and the strengthened frame (RCJF75) are presented in Figure 5.

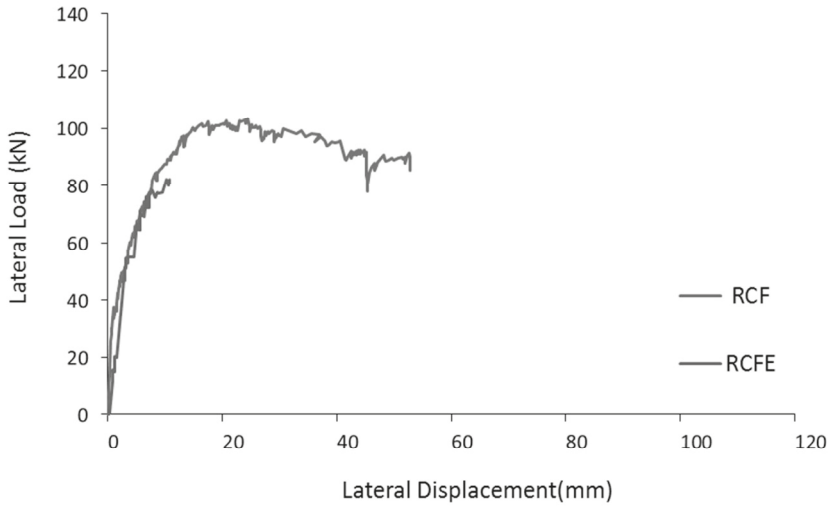


Figure 4 – The load-displacement diagrams for the reference frame RCF and the frame damaged to 75 % of the maximum load of RCF (RCFE).

Table 3 shows a comparison for the behaviours of the RCF and RCJF75 frames. The parameters presented are yielding displacement ( $\Delta_y$ ), ultimate displacement ( $\Delta_u$ ), yielding load of tensile reinforcement ( $P_y$ ), ultimate load ( $P_u$ ) and displacement ductility ( $\mu$ ). The ductility ( $\mu$ ) is defined as the ratio between the ultimate displacement ( $\Delta_u$ ) and the yielding displacement ( $\Delta_y$ );  $\mu = \Delta_u / \Delta_y$ .

Table 3 – Comparison of frames displacements

Specimen	$\Delta_y$ (mm)	$\Delta_u$ (mm)	$P_y$ (kN)	$P_u$ (kN)	$\mu = \Delta_u / \Delta_y$
RCF	7.62	45.25	77.83	103.25	5.94
RCJF75	6.1	97.22	100	120.2	15.9

Comparison of the load-displacement behaviours of the RCF frame and the strengthened frame, RCJF75 indicates that the initial stiffness of both specimens are same up to yielding point (77 kN load). After reaching the yielding point, the strengthened specimen (RCJF75) possesses higher stiffness than the reference specimen (RCF), see Figure 5. In comparison with RCF, the strengthened frame shows an improvement of yielding load (30 %), ultimate load (17 %), and ductility (2.7 times).

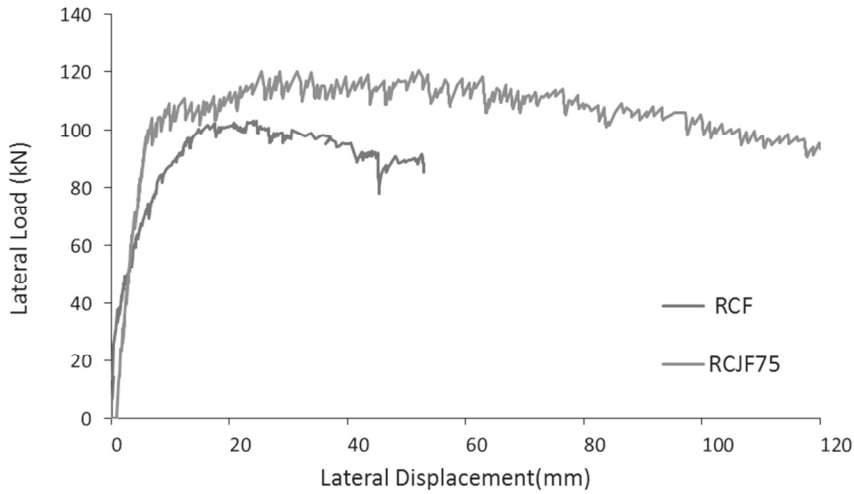


Figure 5 – Experimental load-displacement curves of the reference frame (RCF) and the strengthened frame (RCJF75).

Ductility is an important parameter of structures, because it guarantees the safety of structures when subjected to seismic loads. The ductility factor of a frame is obtained from the load-displacement curve. The ultimate displacement ( $\Delta_u$ ) is measured up to 15 % degradation after the peak point, so no more displacement is required after that point for calculating ductility and hence the  $\Delta_u$  is equal 97.22 mm, see Table 3.

Using HPFRCC in strengthened frame leads to increase in final ductility of the frames. The main reason for improving ductility might be different crack pattern between reference frame (RCF) and strengthened frame (RCJF75). Figure 6 shows the schematic figure of cracks in both RCF and RCJF75 frames. In strengthened frame with HPFRCC concrete ductility is increased approximately 300 % in comparison with reference frame.

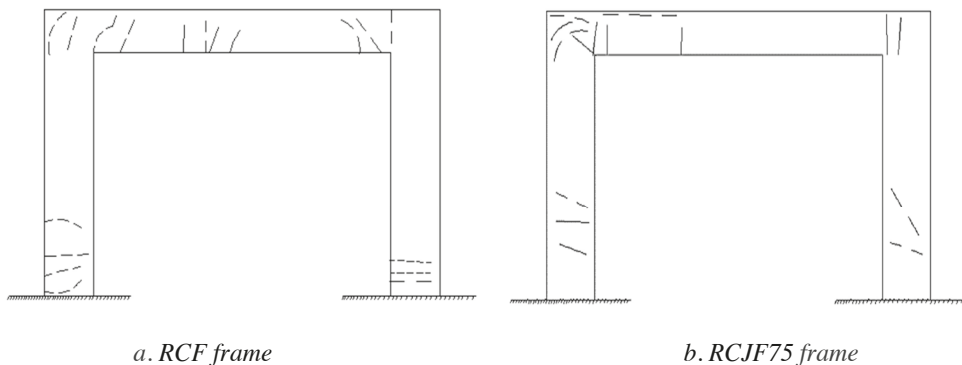


Figure 6 – Schematic cracking patterns of reference frame (RCF) and strengthened frame (RCJF75) at ultimate deflection.

#### 4. CONCLUSION

In this paper, experimental strengthening of damaged frame with high-performance fibre-reinforced cementitious composites (HPFRCC) under lateral and gravity loads is investigated. Reference frame was tested up to its ultimate load capacity, then another frame was tested up to 75 % of its ultimate capacity and while remaining as damaged, strengthening with HPFRCC layer was done at the critical lengths.

Strengthening of RC frame with HPFRCC results in improving of concrete ductility. The main reason for improving ductility might be different crack pattern between reference frame and strengthened frame. Final displacement of the strengthened frame is 2.15 times more than that of the reference frame. Both reference and strengthened specimens indicate the same stiffness up to yielding point. After reaching yielding point, the strengthened specimen possesses higher stiffness than the reference specimen. In comparison with reference frame, the strengthened frame shows an improvement of yielding load (30 %), ultimate load (17 %).

#### REFERENCES

1. Markeset, G., "Comments on Size Dependence and Brittleness of High Strength Concrete", SINTEF Report STF70 A95029, ISBN 82-595-9061-6, 1995, 25 pp.
2. Markeset, G., "Strain Softening and Structural Analysis of Beams Failing in Compression", Fracture Mechanics of Concrete Structures, FRAMCOS-3, (ed Mihashi and Rokugo), AEDICATIO Publisher, ISBN 3-931681-21-1, 1998, pp. 1183-1194.
3. Krenchel, H. and Stang, H. "Stable microcracking in cementitious materials", In Brittle Matrix Composites 2. A.M. Brandt and J.H. Marshall, eds., pp. 20-33, 1989.
4. Markeset, G. & Jensen, J. J., "Reinforced High Strength Concrete Slabs Exposed to Impact Loadings", High Strength Concrete, Proceedings, First International Conference, Kona Hawaii, ASCE publisher, ISBN 0-7844-0419-4, Kona, Hawaii, 1997, pp. 52-64.
5. Jensen, J. J., Tomaszewics A. & Markeset, G., "Impact Resistance of Fiber Reinforced High Strengt Concrete Slabs", Proceedings, Concrete under Severe Conditions 2, CONSEC'98, Tromsø, Norway, E & FN Spon, ISBN 0-419-23880-6-8, 1998, pp. 795-804.
6. Alaei, Farshid Jandaghi. Retrofitting of concrete structures using high performance fibre reinforced cementitious composite (HPFRCC). Diss. Cardiff University, 2002.
7. Rokugo, Keitetsu, et al. "Applications and recommendations of high performance fiber reinforced cement composites with multiple fine cracking (HPFRCC) in Japan." *Materials and structures* 42.9 (2009): 1197-1208.
8. Ilki, Alper, et al. "Seismic retrofit of brittle and low strength RC columns using fiber reinforced polymer and cementitious composites." *Advances in Structural Engineering* 12.3 (2009): 325-347.
9. Martinola, Giovanni, et al. "Strengthening and repair of RC beams with fiber reinforced concrete." *Cement and Concrete Composites* 32.9 (2010): 731-739.
10. Hung, Chung-Chan, and Yu-Syuan Chen. "Innovative ECC jacketing for retrofitting shear-deficient RC members." *Construction and Building Materials* 111 (2016): 408-418.
11. Choi, Won-Chang, et al. "Attempts to apply high performance fiber-reinforced cement composite (HPFRCC) to infrastructures in South Korea." *Composite Structures* 109 (2014): 211-223.

12. Naaman, A.E. and Reinhardt, H.W. Setting the stage: toward performance-based classification of FRC composites, In High Performance Fiber Reinforced Cement Composites (HPFRCC-4), Proc. of the 4th Int'l RILEM Workshop, A.E. Naaman and H.W. Reinhardt, eds. Published by RILEM S.A.R.L., (2003)
13. Bache, H. Densified cement/ultra-fine particle-based materials, CBL Rapport No. 40, Aalborg Portland, ISBN 87-89132-00-9, (1981).
14. Chanvillard, G. and Rigaud, S. Complete characterization of tensile properties of ductal UHPFRC according to the French recommendations, In Proc. of High Performance Fiber Reinforced Cement Composites (HPFRCC4), A.E. Naaman and H.W. Reinhardt, eds, pp. 21-34. RILEM Publications S.A.R.L., (2003)
15. Li, V.C. "From Micromechanics to Structural Engineering – the design of cementitious composites for Civil Engineering applications", JSCE J. of Struc. Mechanics and Earthquake Engineering 10(2), pp.37-48, 1993.
16. Fischer, G., Wang, S. and Li, V.C. "Design of engineered cementitious composites for processing and workability requirements", Seventh International Symposium on Brittle Matrix Composites, pp. 29- 36. Warsaw, Poland, 2003.
17. Reinhardt, H.W., Krüger, M. and Große, C.U. "Concrete prestressed with textile fabric", Journal of Advanced Concrete Technology 1(3), pp. 231-239, 2003.
18. Hemmati, A., kheyroddin, A., Sharbatdar, M K., "Plastic hinge rotation capacity of reinforced HPFRCC beam" Journal of Structural engineering, ASCE. Volume 141, Issue 2 (2015).
19. Hemmati, A., Kheyroddin,A., Sharbatdar, M. Kazem; Park, Y., Abolmaali, A. "Ductile behavior of high performance fiber reinforced cementitious composite (HPFRCC) frames", Construction & Building Materials, 2016.
20. Li,V., Fischer,G., "Effect of matrix ductility on Deformation Behavior of Steel Reinforced ECC Flexural Member Under Cyclic Loading Condition", ACI Structural Journal. 2002.
21. Parra-Montesinos, G. J., "High-Performance Fiber-Reinforced Cement Composites: An Alternative for Seismic Design of Structures," ACI Structural Journal, V. 102, No. 5, September-October 2005, pp. 668-675.
22. Sharbatdar, M. Kazem , Kheyroddin, A., Emami, E., "Cyclic performance of retrofitted reinforced concrete beam–column joints using steel prop", Construction and Building Materials 36 (2012) 287–294, <http://dx.doi.org/10.1016/j.conbuildmat.2012.04.115>.

## Investigation of the seismic response of reinforced concrete column-beam connections using high performance fibre reinforced cementitious composites (HPFRCC)



Mahdi Kioumars  
Associate Professor  
Oslo and Akershus University College of Applied Sciences  
Department of Civil Engineering and Energy Technology  
Pilestredet 35, Oslo  
E-mail: [mahdi.kioumars@hioa.no](mailto:mahdi.kioumars@hioa.no)



Mahdi Tajfar  
Graduate Student of Department of Civil Engineering, Semnan  
Branch, Islamic Azad University, Semnan, Iran  
E-mail: [mahdi\\_tajfar@yahoo.com](mailto:mahdi_tajfar@yahoo.com)



Ali Kheyroddin  
Professor  
Semnan University, Department of Civil Engineering  
E-mail: [kheyroddin@semnan.ac.ir](mailto:kheyroddin@semnan.ac.ir)



Benyamin Kioumars  
Ph.D candidate  
Semnan University, Department of Civil Engineering  
E-mail: [benyamin.kioumars@gmail.com](mailto:benyamin.kioumars@gmail.com)

### ABSTRACT

In this paper, the effect of using high-performance fibre-reinforced cementitious composites (HPFRCC) on behaviour of reinforced concrete beam-column connection is investigated. The external beam-column connection of ordinary reinforced concrete experimentally tested by Fernandes was selected for validation. The effect of strengthening of connection with different lengths of HPFRCC in beam and column is investigated using nonlinear finite element analysis (NLFEA). Based on the obtained results, optimum connections that have maximum strength, maximum ductility, or maximum energy absorption are introduced.

**Key words:** High-performance fibre-reinforced cementitious composites, Reinforced concrete, beam-column connection, ductility, energy absorption, finite element method.

### 1. INTRODUCTION

Today, most reinforced concrete (RC) buildings in Europe and around the world are decades old and have been damaged due to different causes. The application of concrete as

a high quality construction material for retrofitting the structures exposed to severe loading conditions was introduced by the development and production of high strength concrete (HSC)/high performance concrete (HPC). Since mid-seventies, there has been a huge increase in the use of HSC/HPC in offshore and bridge construction in Norway and elsewhere. However, the increased compressive strength obtained by reducing the water-cement ratio to 0.40 (or somewhat lower), leads to a more brittle material behaviour compared to normal strength concrete [1, 2]. For concrete structures exposed to severe dynamic loadings, like impact and earthquake, ductile structural response is of importance. By adding steel fibres to the concrete mix of HSC, the tensile properties could be increased substantially [3].

Another solution that has been proposed for retrofitting concrete structures, is the use of high-performance fibre-reinforced cementitious composites (HPFRCC) [4-9]. HPFRCC can be classified as a high-strength material depending on the stress-strain characteristic of the composite included. If the stress-strain diagram indicates strain hardening after initial cracking, then the composite is classified as a high-strength material. Otherwise, the material is termed an ordinary fibre-reinforced composite (FRC) the stress-strain diagram of which exhibits strain softening immediately after initial cracking. Therefore, HPFRCC is a special type of FRC which, under tension, exhibits strain hardening after initial cracking, accompanied by multiple cracks before relatively high strains are developed [10].

In recent years, two types of HPFRCC have been introduced: Ductal® composites and engineering cementitious composites (ECC). The former is the result of research conducted in 1981 [11]. A stiff dense mortar as well as high-strength fibres is used to produce this type of composite. A strong bond is created between the fibres and the mortar due to the high strength of the mortar, leading to high material strength after cracking. By using high strength fibres, this type of composite can be designed for elastic applications where fibres play a significant role under extreme conditions by tolerating tensile loads. According to the research conducted in 2003 [12], the tensile strength and ductility of this composite are 12 MPa and 0.02-0.06 percent, respectively.

The ECC are designed as both elastic and plastic materials. The fibres embedded in these materials enable them to effectively behave under serviceability and ultimate limit conditions. The strength and ductility of ECC under tension are 4-6 MPa and 3-5 percent respectively [13, 14]. Different ECC can be used in different applications including the following: a) Self Consolidating ECC: these are used for large-scale concreting operations as well as concreting in areas where heavy reinforcement is to be implemented, b) Light Weight ECC: this type is used for reducing structural dead load, c) Green ECC: used for reducing environmental hazards and promoting sustained development, and d) Self-repairing ECC: also termed "self-healing", these ECCs are used for improving/retrofitting the mechanical characteristics of materials which have sustained damage [15-19].

With regards to the above discussion, HPFRCC is an appropriate substitute material for strengthening RC connection which has been made by ordinary concrete. However, according to authors' knowledge, more investigations are required to find the optimum strengthened length of beam and column. In this paper, after verifying nonlinear response of finite element model (FEM) with selected experimental case, effect of different parameters on nonlinear behaviour of beam-column connection are discussed. The parameters are the lengths of HPFRCC used in beams or columns and at the same time in

beams and columns. Based on the obtained results, optimum connections that have maximum strength, maximum ductility, or maximum energy absorption are introduced.

## 2. NONLINEAR FINITE ELEMENT ANALYSIS (NLFEA)

### 2.1 Finite element software

In this study, nonlinear finite element software ABAQUS is used for analysing nonlinear behaviour of RC connection under cyclic load. Three structural methods are included in ABAQUS for such modelling: 1) the smeared crack concrete model, 2) the brittle cracking model, and 3) the concrete damage plasticity model [20]. The first model is used for concrete structures under monotonic loading. In this model, the concrete is subjected to either tension or compression cracking. The last is due to dilatation strains in the concrete volume in compression. The concrete damage plasticity model is based on the assumptions applied for isotropic concrete deterioration, and can be used for concrete structures under different loading conditions including cyclic loading. This model considers the effect of elastic hardening resulting from tension/compression plastic strain as well as the effect of improved material stiffness under cyclic loading. Due to the specific behaviour of HPRFCCs in tension, the concrete damage plasticity model was selected for the concrete.

### 2.2 Simulation of selected experimental case

In this study, the external beam-column connection of ordinary reinforced concrete experimentally tested by Fernandes [21] was selected for validation. Figures 1 and 2 show the dimensions as well as reinforcement and loading details of this connection. To include the effect of axial force in the connection behaviour, a compressive force of 220 kN (equal to 10% of the load carrying capacity of the column) was introduced in the column for simulating the test setup. At the end of the beam, a roller support, and at the lower end of the column, a fixed hinged support were installed. The upper end of the column was braced against movement in the plane vertical to the connection. A 500 kN hydraulic jack capable of cyclic loading was used to provide the required displacement in the connection plane.

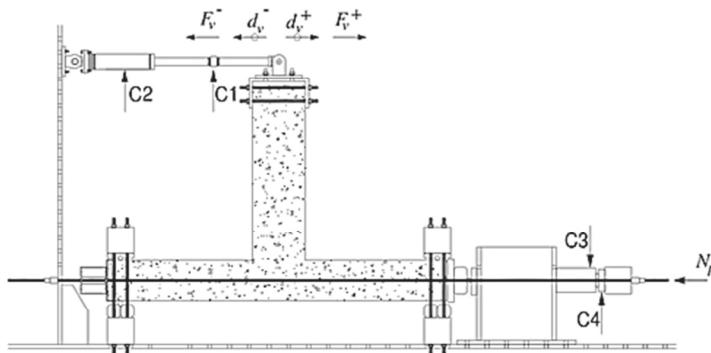


Figure 1 – Detail of loading in RC connection, experimented by Fernandes [21].



The experimental reference model used in the tests was called REF. The “HC” term used in a model name shows that the model is a combination of ordinary concrete and a HPFRCC material.

*Table 1 – NLFE Models specifications*

FE model	NLFE model of Beam-column connection
REF	Whole connection is modelled by ordinary concrete
HC-B20	200 mm of beam is modelled by HPFRCC, the rest is ordinary concrete
HC-B40	400 mm of beam is modelled by HPFRCC, the rest is ordinary concrete
HC-B80	800 mm of beam is modelled by HPFRCC, the rest is ordinary concrete
HC-B100	1000 mm of beam is modelled by HPFRCC, the rest is ordinary concrete
HC-C40	400 mm of column is modelled by HPFRCC, the rest is ordinary concrete
HC-C80	800 mm of column is modelled by HPFRCC, the rest is ordinary concrete
HC-C100	1000 mm of column is modelled by HPFRCC, the rest is ordinary concrete
HC-B80-C40	800 mm of beam and 400mm of column are modelled by HPFRCC, the rest is ordinary concrete
HC-B80-C80	800 mm of beam and 800mm of column are modelled by HPFRCC, the rest is ordinary concrete
HC-B80-C120	800 mm of beam and 1200mm of column are modelled by HPFRCC, the rest is ordinary concrete
HPFRCC	Whole connection is modelled by HPFRCC

#### 4. RESULTS AND DISCUSSION

Figures 4-7 show the hysteresis envelope curves of models after NLFEA. Summary of obtained results of NLFEA are presented in Table 2. The following parameters are considered to be presented in Table 2:

$P_y$ : Yield load

$\delta_y$ : Displacement corresponding to the yield load ( $P_y$ )

$P_u$ : Ultimate load of connection

$\delta_u$ : Displacement corresponding to ultimate load ( $P_u$ )

$\mu$ : Ductility, defined as the ratio  $\delta_u$  over  $\delta_y$

$P_{max}$ : Maximum load of connection

$\delta_{max}$ : Displacement corresponding to ( $P_{max}$ )

$P_{cr}$ : Cracking load of connection

$\delta_{cr}$ : Displacement corresponding to ( $P_{cr}$ )

*Table 2 – Summary of obtained results of NLFEA for different models*

FE model	$P_y$	$\delta_y$	Drift y	$P_u$	$\delta_u$	Drift u	$\mu$	$P_{max}$	$\delta_{max}$	$P_{max}/P_y$	$P_{cr}$	$\delta_{cr}$	$E_{abs}$
	kN	mm	%	kN	mm	%		kN	mm		kN	mm	kJ
REF	26.13	38.98	2.9	61.8	122.97	9.1	3.15	72.71	115.2	2.783	26.41	2.2	125332
HC-B40	27.4	23.90	1.8	61.87	128.50	9.5	5.37	72.80	109.8	2.657	40.40	2.33	123765
HC-B80	25.78	18.55	1.4	63.34	133.20	9.9	7.18	74.50	112.6	2.891	36.12	2.2	160967
HC-B100	25.12	21.92	1.6	62.68	124.60	9.2	5.68	73.70	101.2	2.936	22	1.15	120812
HC-C40	25.21	19.11	1.4	64.15	150.30	11.1	7.86	75.47	100.6	2.994	23.88	1.87	226773
HC-C80	24.96	20.11	1.5	62.63	160.90	11.90	8	73.68	90.04	2.952	33.3	2.17	223782
HC-C100	28.84	20.23	1.5	62.37	153.60	11.4	7.59	73.38	73.73	2.544	16.94	1.62	225802
HC-B80-C0	25.78	18.55	1.4	63.34	133.20	9.9	7.18	74.50	112.6	2.891	36.12	2.2	160967
HC-B80-C40	45.99	20	1.5	70.87	131.90	9.8	6.59	83.28	62.58	1.811	48.81	2.42	199948
HC-B80-C80	74.68	18.75	1.4	74.24	147.70	10.9	7.88	87.34	25.04	1.170	26.8	0.62	230907
HC-B80-C120	89.87	20.7	1.5	78.01	138.60	10.3	6.70	91.78	12.12	1.021	48.28	2.05	248041
HPFRCC	92.24	17.77	1.3	84.98	138.43	10.3	7.79	99.98	12.97	1.084	78.34	11.55	267729

#### 4.1 Models where HPFTCC is added to the beam

According to Figure 4 and Table 2, the greatest ductility for the HPFRCC materials in the beam was obtained at a HPFRCC length equal to twice the beam depth (800 mm) where the connection ductility was 7.18, i.e., 127% greater than that in the reference connection (REF). Therefore, it can be concluded that the ductility trend followed by the HPFRCC materials was, as expected, very favourable. The best hysteresis envelope curves for this case were obtained at Connection HC-B80. Figure 5 depicts the collapse and cracking pattern obtained for Connection HC-B80.

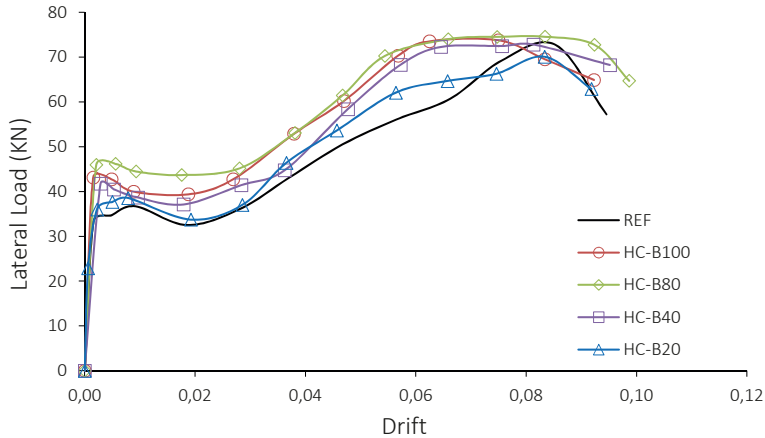


Figure 4 – Hysteresis envelope curves at four different HPFRCC lengths in the beam, see models HC-B20, HC-B40, HC-B80, and HC-B100 in Table 1.

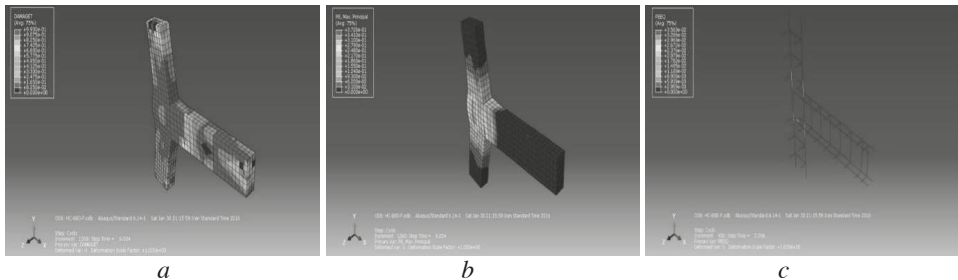


Figure 5 – Collapse and cracking patterns for Model HC-B80; a) tensile damage pattern in under ultimate load (63.34 kN), b) crack pattern in terms of maximum principle tensile strains under ultimate load (63.34 kN), and c) yielding threshold pattern in terms of equivalent plastic strain under yielding load (25.78 kN).

#### 4.2 Models where HPFRCC is added to the column

According to Figure 6 and Table 2, increasing the HPFRCC length in the column caused only a slight corresponding increase in maximum load, ultimate load, and yield load of the connection as compared with the reference (REF) connection, with increases of 10% in yield load of

Connection HC-C100, as well as 4% and 4% in maximum and ultimate loads of Connection HC-C40 respectively.

Increasing the length of the HPFRCC area in the column greatly improved the connection ductility, producing increase of 149.3%, 154%, and 141% in Connections HB-BC40, HC-C80, and HC-C100 as compared with the reference connection (RFE), respectively. Increasing the HPFRCC length from 800 mm to 1000 mm caused a corresponding decrease in the ductility ratio, with Model HC-C100 experiencing a 9% reduction as compared with Model HC-BC80. In Models HC-C40, HC-B80, and HC-B100, the energy absorption percentages were 81%, 79%, and 80%, respectively. Thus, it is concluded that Connection HC-C80 behaves suitably in terms of ductility. Another conclusion was that using HPFRCC materials in the column led to a corresponding increase in the ductility ratio (unlike the case where HPFRCC materials were used in the beam alone). Figure 7 depicts the collapse and cracking pattern for Connection HC-C80.

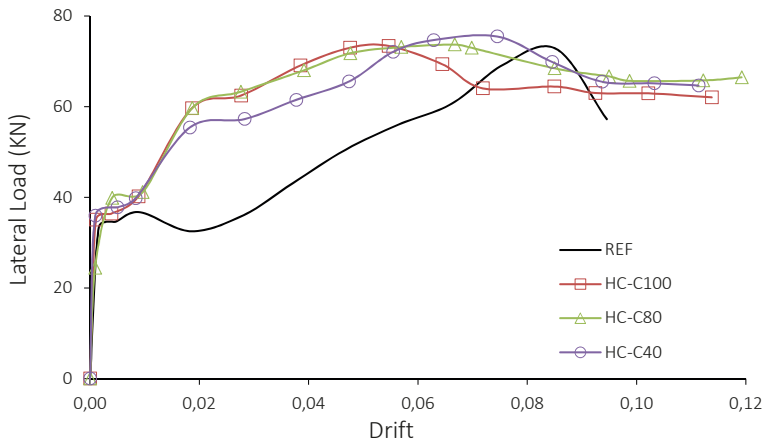


Figure 6 – Hysteresis envelope curves at three different HPFRCC lengths in the column, see models HC-C0, HC-C80, and HC-C100 in Table 1.

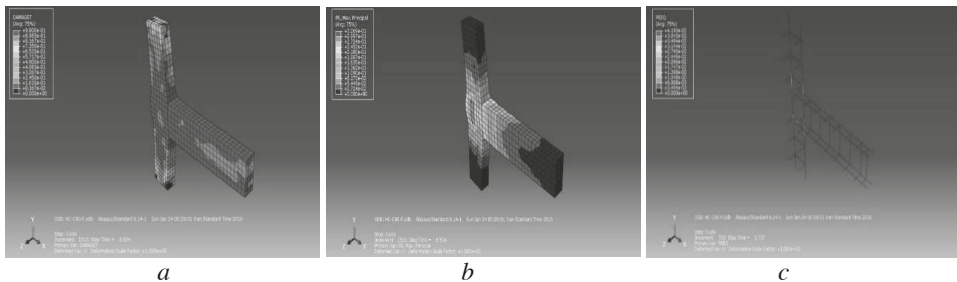


Figure 7 – Collapse and strain patterns for Model HC-C80; a) tensile damage pattern in terms of tensile stress under ultimate load (62.63 kN), b) crack pattern in terms of maximum principle tensile strains under ultimate load (62.63 kN), and c) yielding threshold pattern in terms of equivalent plastic strain under yielding load (24.96 kN).

### 4.3 Models where HPFRCC is added both in beam and column

Figure 8 and Table 2 show that using HPFRCC materials in both the beam and the column increased the yield strength, the maximum strength, and the ductility of the connection as compared with the reference connection. Accordingly, as compared with the reference model REF, Models HC-B40-C80, HC-B80-C80, and HC-B80-C120 experienced yield load increases of 76, 186, and 244 percent, maximum load increases of 14, 20, and 26 percent, and ultimate load increases of 14, 20, and 26 percent respectively.

Increasing the HPFRCC length also led to a corresponding increase in ductility, with 109, 149, and 112 percent increases in Models HC-B80-C40, HC-B80-C80, and HC-B80-C120 respectively. In addition, the percent energy absorption increase as a result of increasing the HPFRCC length in the column, with Models HC-B80-C40, HC-B80-C80, and HC-B80-C120 showing increases in energy absorption of 50, 84, and 98 percent respectively (as compared with REF).

Therefore, it is concluded that using HPFRCC materials in the column when these materials are already used in the beam would considerably influence the beam-column connection strength as well as ductility. For this reason, reinforcing the beam alone is not sufficient and the supporting columns should also be reinforced. On the other hand, as the ductility of Connection HC-B80-C120 exhibited a 35% decrease as compared with Connection HC-B80-C80, increasing the HPFRCC length beyond 800 mm would not be advisable. Figure 9 and 10 depict the collapse and cracking patterns of Connection HC-B80-C80 and HC-B80-C120.

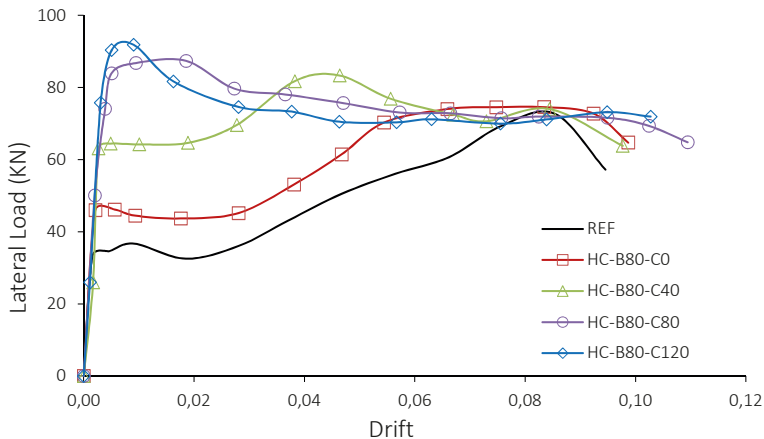


Figure 8 – Hysteresis envelope curves developed at four different HPFRCC lengths in the column constant HPFRCC length in the beam, see models HC-B80, HC-B80-C40, HC-B80-C80, and HC-B80-C120 in Table 1.

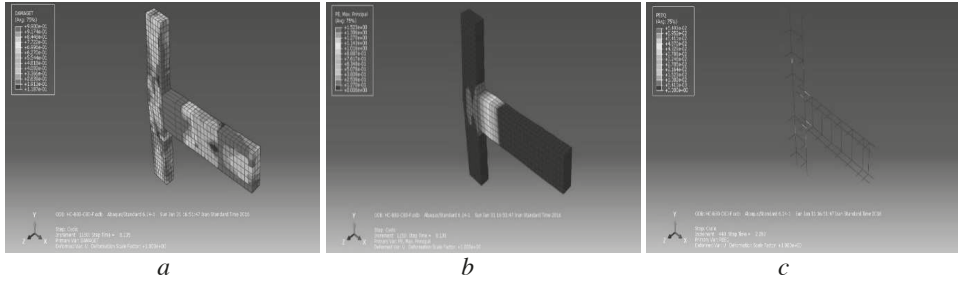


Figure 9 – Collapse and strain patterns for Model HC-B80-C80; a) tensile damage pattern in terms of tensile stress under ultimate load (74.24 kN), b) crack pattern in terms of maximum principle tensile strains under ultimate load (74.24 kN), and c) yielding threshold pattern in terms of equivalent plastic strain under yielding load (74.68 kN).

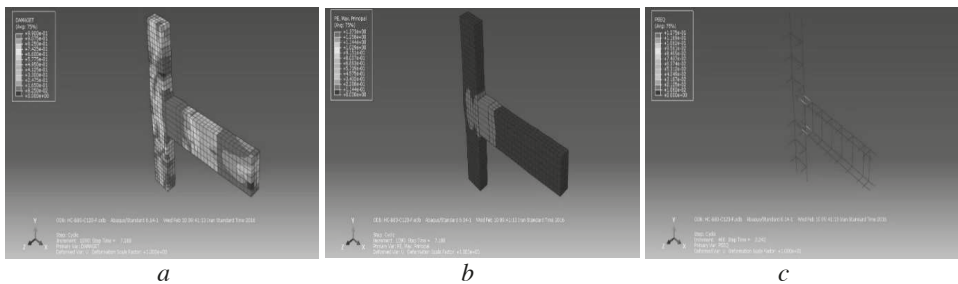


Figure 10 – Collapse and strain patterns for Model HC-B80-C120; a) tensile damage pattern in terms of tensile stress under ultimate load (78.01 kN), b) crack pattern in terms of maximum principle tensile strains under ultimate load (78.01 kN), and c) yielding threshold pattern in terms of equivalent plastic strain under yielding load (89.87 kN).

#### 4.4 Models where HPFRCC is added in entire connection

As shown in Figure 11 and Table 2, the strength of the connection made entirely of HPFRCC materials is an improvement as compared to the reference connection; the yield, maximum and ultimate loads increasing by 253, 38, and 38 percent respectively. In addition, the ductility ratio and the percentage of absorbed energy in the connections made entirely of HPFRCC materials increased by 147 and 114 percent respectively (as compared with REF). Therefore, it might be concluded that a connection made fully of HPFRCC materials has increased strength and ductility. However, because the strength and ductility obtained for Connection HC-B80-C80 are more or less similar to those obtained for the connection made of HPFRCC materials alone, using a pure HPFRCC connection would not be economical.

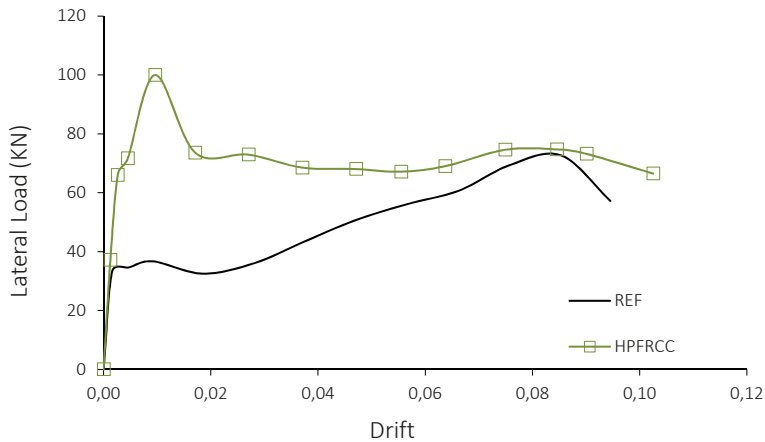


Figure 11 – Hysteresis envelope curves developed at the connection with HPMRCC materials, see model HPMRCC in Table 1.

#### 4.5 Optimum connection in bending

To find the optimum connection in bending, all the studied models were compared, assuming a specific connection as the optimum design due to its maximum resistance, ductility or energy absorption. The selected models with the maximum mentioned responses are HC-C80, HC-B80-C80, HC-B80-C120, and HPMRCC. Figure 12 presents a comparison of hysteresis curve envelopes obtained for the selected connections.

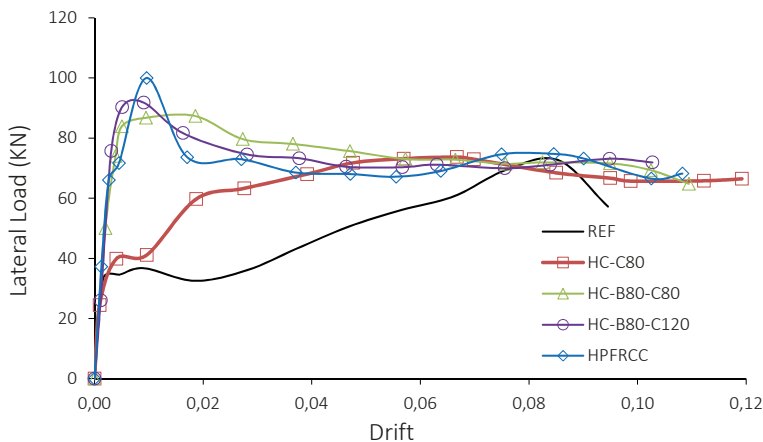


Figure 12 – Comparison of hysteresis curve envelopes for Models HC-C80, HC-B80-C80, HC-B80-C120, and HPMRCC to find the optimum connections in bending.

With due consideration of Figure 12 and Table 2, it can be stated that the maximum strength in the HPMRCC connection (including HPMRCC connections, beam, and column) was 99.98 kN/m<sup>2</sup>, i.e., 27% more than that in reference connection. The maximum strength in Connection

HC-B80-C120 (with constant HPFRCC lengths of 800 and 1200 mm in beam and column respectively and the rest of the connection made of ordinary concrete) was  $91.78 \text{ kN/m}^2$ , i.e., 37% more than that in the reference connection. The maximum strength in Connection HC-B80-C80 (with constant HPFRCC lengths of 800 mm in both beam and column and the rest of the connection made of ordinary concrete) was  $87.34 \text{ kN/m}^2$ , i.e., 20% more than that in the reference connection. In addition, the maximum strengths in these three models were higher than those obtained for the other models. As such, these three models can be considered as optimum designs in terms of maximum strength.

The ductility ratios obtained for Models HC-C80, HC-B80-C80, and HPFRCC were 8, 7.88, and 7.79, being 154, 150, and 147 percent greater than those obtained for the reference connection respectively. These models are thus optimal in terms of maximum ductility.

Energy absorption values obtained for Models HPFRCC, HC-B80-C120, and HC-B80-C80 were 267729, 248041, and 230908 kJ, respectively, corresponding to increases of 114, 98, and 84 percent as compared with the reference connection. Therefore, these three models can be introduced as optimum models in terms of energy absorption.

A review of the above factors leads to the conclusion that Models HPFRCC and HC-B80-C80 can be regarded as optimum models in terms of beam-column connection bending. However, in terms of cost, Connection HC-B80-C80 would definitely be the best choice due to the fact that less HPFRCC material is used therein.

#### 4. CONCLUSION

The strain hardening under tension behaviour in HPFRCC, makes this composite drastically different from other cementitious and concrete composites, turning it into a high-strength material with high energy absorption that can withstand multiple pre-failure crackings. In recent years, HPFRCC concretes (also called “high-strength concretes”) have been considered for retrofitting structures against seismic loading. One characteristic of HPFRCC which makes them particularly suitable for substituting ordinary concrete in retrofitting operations is that, being structurally similar to concrete, HPFRCC can create a strong bond with the old concrete parts in the building. The following results were obtained in the present study:

- Strengthening the plastic hinge area developing in the beam, by using HPFRCC, increases the maximum strength, ultimate strength, and ductility of the connection.
- Simultaneous strengthening of the plastic hinge area in the beam and column improves the behaviour of the connection as compared to the case where only the beam is strengthened.
- The most suitable strengthened length in the column is equal to that in the beam. Increasing the strengthened length in the column beyond that in the beam might even reduce connection ductility.
- The plastic hinge location can be transferred from the column to the beam by using HPFRCC only in the column or simultaneously using HPFRCCs in the beam and column or building the connection entirely of HPFRCC. However, if the beam is made entirely of HPFRCC, then the plastic hinge will be formed in the column.
- Using HPFRCC in the column alone favourably increases energy absorption as compared with the reference model. However, using these materials in the beam alone

led to reduced energy absorption as compared with the reference model. This was particularly true in Models HC-B40 and HC-B100.

- Increasing the HPFRCC length in the beam alone from twice the beam depth (800mm) to 2.5 times the beam depth (1000mm) had a slight effect on the connection strength, but reduced connection ductility by 37%.
- Connection HC-B80-C80 (wherein less HPFRCC was used) exhibited maximum strength, ductility ratio, energy absorption, and cost factors that made it the optimum solution beam-column bending connections as compared to the connection made entirely of HPFRCC materials.
- Substitution of ordinary concrete with its equivalent HPFRCC material, in lengths twice the beam depth both in the beam and column, would increase the yield strength and the maximum strength, as well as the ductility and energy absorption characteristics in the RC connection (RC frame). Therefore, strengthening a connection with HPFRCC in excess of twice the beam depth is not recommended as an economical solution.

## REFERENCES

1. Markeset, G., "Comments on Size Dependence and Brittleness of High Strength Concrete", SINTEF Report STF70 A95029, ISBN 82-595-9061-6, 1995, 25 pp.
2. Markeset, G., "Strain Softening and Structural Analysis of Beams Failing in Compression", Fracture Mechanics of Concrete Structures, FRAMCOS-3, (ed Mihashi and Rokugo), AEDICATIO Publisher, ISBN 3-931681-21-1, 1998, pp. 1183-1194.
3. Krenchel, H. and Stang, H. "Stable microcracking in cementitious materials", In Brittle Matrix Composites 2. A.M. Brandt and J.H. Marshall, eds., pp. 20-33, 1989.
4. Alaei, Farshid Jandaghi. Retrofitting of concrete structures using high performance fibre reinforced cementitious composite (HPFRCC). Diss. Cardiff University, 2002.
5. Rokugo, Keitetsu, et al. "Applications and recommendations of high performance fiber reinforced cement composites with multiple fine cracking (HPFRCC) in Japan." *Materials and structures* 42.9 (2009): 1197-1208.
6. Ilki, Alper, et al. "Seismic retrofit of brittle and low strength RC columns using fiber reinforced polymer and cementitious composites." *Advances in Structural Engineering* 12.3 (2009): 325-347.
7. Martinola, Giovanni, et al. "Strengthening and repair of RC beams with fiber reinforced concrete." *Cement and Concrete Composites* 32.9 (2010): 731-739.
8. Hung, Chung-Chan, and Yu-Syuan Chen. "Innovative ECC jacketing for retrofitting shear-deficient RC members." *Construction and Building Materials* 111 (2016): 408-418.
9. Choi, Won-Chang, et al. "Attempts to apply high performance fiber-reinforced cement composite (HPFRCC) to infrastructures in South Korea." *Composite Structures* 109 (2014): 211-223.
10. Naaman, A.E. and Reinhardt, H.W. Setting the stage: toward performance-based classification of FRC composites, In High Performance Fiber Reinforced Cement Composites (HPFRCC-4), Proc. of the 4th Int'l RILEM Workshop, A.E. Naaman and H.W. Reinhardt, eds. Published by RILEM S.A.R.L., (2003)
11. Bache, H. Densified cement/ultra-fine particle-based materials, CBL Rapport No. 40, Aalborg Portland, ISBN 87-89132-00-9, (1981).
12. Chanvillard, G. and Rigaud, S. Complete characterization of tensile properties of ductal UHPFRC according to the French recommendations, In Proc. of High Performance Fiber Reinforced Cement Composites (HPFRCC4), A.E. Naaman and H.W. Reinhardt, eds, pp. 21-34. RILEM Publications S.A.R.L., (2003)

13. Li, V.C. From Micromechanics to Structural Engineering – the design of cementitious composites for Civil Engineering applications, *JSCE J. of Struc. Mechanics and Earthquake Engineering* 10(2), pp.37-48, (1993).
14. Fischer, G., Wang, S. and Li, V.C. Design of engineered cementitious composites for processing and workability requirements, *Seventh International Symposium on Brittle Matrix Composites*, pp. 29-36. Warsaw, Poland, (2003).
15. Kong, H.J., Bike, S. and Li, V.C. Development of a self-compacting engineered cementitious composite employing electrostatic dispersion/stabilization, *Journal of Cement and Concrete Composites* 25(3), pp. 301-309, (2003).
16. Lepech, M.D. and Li, V.C. Large scale processing of engineered cementitious composites, *ACI Materials Journal*, (2007).
17. Wang, S. and Li, V.C. High early strength engineered cementitious composites", *ACI Materials Journal*, 103(2), pp. 97-105, (2006).
18. Yang, Y., Lepech, M. and Li, V.C. Self-healing of engineered cementitious composites under cyclic wetting and drying. In *Proc. Int. Workshop on Durability of Reinforced Concrete under Combined Mechanical and Climatic Loads (CMCL)*, pp. 231-242. Qingdao, China, (2005).
19. Li, V.C. and Yang, E.H. Self-healing in concrete materials. In *Self-Healing Materials: An Alternative Approach to 20 Centuries of Materials Science*, S. van der Zwaag, ed., pp. 161–193, (2007).
20. Abaqus, User Manual ver. "6.14." Providence: Hibbit Karlsson and Sorensen (2015).
21. Fernandes P. and Sena-Cruz J. (2012), "Efficiency of Different Techniques in Seismic Strengthening of RC Beam-Column Joints", *Materials and Structures*.

## Fatigue Analysis of RC Beams Strengthened in Flexure using CFRP

Mohammed Mahal

Ph.D.

Luleå University of Technology

Dept. of Structural Engineering

SE – 971 87 Luleå

Department of Civil Engineering, Mosul University, Mosul, Iraq

E-mail: [mohammed.salih@ltu.se](mailto:mohammed.salih@ltu.se)

Dr. Björn Täljsten

Professor

Luleå University of Technology

Dept. of Structural Engineering

SE – 971 87 Luleå

Sto Scandinavia AB, Sweden

E-mail: [bjorn.taljsten@ltu.se](mailto:bjorn.taljsten@ltu.se)

Dr. Thomas Blanksvärd

Associate Senior Lecturer

Luleå University of Technology

Dept. of Structural Engineering

SE – 971 87 Luleå

E-mail: [thomas.blanksvard@ltu.se](mailto:thomas.blanksvard@ltu.se)

### ABSTRACT

The increasing use of Fiber Reinforced Polymers (FRP) to repair, strengthen or upgrade reinforced concrete (RC) structural elements means that there is a need to develop analytical methods for analyzing the behavior of strengthened members under fatigue loading. This paper describes an analytical model for simulating the fatigue behavior of RC beams strengthened with Carbon Fiber Reinforced Polymer (CFRP). Fatigue calculations are performed using a lamellar model that considers the fatigue behavior of the RC and CFRP strengthening materials during loading. The model's output is compared to experimental data for four CFRP-strengthened beams, showing that the new model accurately predicted the deflection and strain of each one. In addition, various models for predicting the fatigue life of CFRP-strengthened RC beams were tested and a model capable of providing conservative fatigue life estimates was identified.

**Keywords:** Analysis, test, fatigue, reinforced concrete, strengthening, fiber reinforced polymer

## 1. INTRODUCTION

In recent decades, fiber-reinforced polymer composites have been used successfully to strengthen diverse concrete structural elements. This is partly because of the desirable material properties of the reinforcing fibers: they exhibit high stiffness and strength, are lightweight, do not corrode, are easily installed, and can be obtained in almost any size or length that may be required. The design and analysis of durable concrete structures requires the consideration of all possible deterioration mechanisms, including both time- and cycle-dependent effects. Fatigue loading is one of these effects and can have significant effects on overall structural performance.

The fatigue behavior of RC beams strengthened with CFRP has received relatively little attention compared to their behavior under static loading conditions. Recent publications have described the behavior of RC beams strengthened with FRP materials under fatigue loading [1-4]. In the last of these reports, it was concluded that strengthened beams tolerated fatigue loading significantly better than unstrengthened reference beams over the same load ranges. It was also noted that the mechanical properties of the beams' components were modified by fatigue loading, which caused a permanent increase in strain and reduced stiffness.

The failure of CFRP-strengthened RC members in flexure appears to be governed by the fatigue rupture of the internal reinforcement. Even under high initial compressive stresses that might be expected to fatigue the concrete, reinforced members fail systematically due to the brittle fatigue fracture of the tensile steel reinforcing bars [5]. This is due to concrete's high capacity for stress redistribution [6]. It is therefore recommended [2] that the stress ranges of the rebars used in strengthened members should not exceed those permitted for unstrengthened RC members.

Theoretical models based on a variety of approaches have been developed to predict the effects of fatigue on strengthened RC beams. Most of the models presented in the literature are based on S-N curves and the static stress state [7-9]. This approach focuses on the number of cycles to failure without considering the redistribution process or the evolution of strain, and thus cannot adequately describe the influence of fatigue on the response of the RC.

Alternative theoretical models are based on damage theory, in which it is assumed that the rate of damage accumulation is independent of the level of applied stress. However, this cannot be true because the material response is greatly influenced by the magnitude of the applied load. Additionally, the assumption of linear damage in this theory ignores the effects of loading sequence. Predictions generated using this model diverged significantly from experimental results [10-12].

Finally, models based on the lamellar technique account for the fatigue of strengthened reinforced concrete beams by dividing the member's cross section into a series of discrete lamellae or segments, each of which is described separately using a uniaxial fatigue stress model. This approach produces accurate predictions, is easy to understand, and has facilitated analyses of the development of stresses and strains during the fatigue life of various structures and predictions of their ultimate failure modes based on their capacity for stress redistribution [13,14].

This work describes a sectional lamellar model for the analysis of CFRP-strengthened reinforced concrete beams under fatigue loading. The model is based on the uniaxial fatigue properties of the concrete and CFRP material under fatigue loading as well as the known stress and strain responses of concrete, CFRP and steel under static loading. The analytical results are compared to experimental data generated by the authors. The model is simple and accurately

describes the overall response of strengthened reinforced concrete beams as well as the development of stresses and strains during fatigue loading.

## 2. FATIGUE MODELS

The behavior of RC structures subjected to fatigue loading is very complex. The mechanical and deformation properties of RC beam components change significantly as the time spend under fatigue loading increases, generating residual strains. Multiple analytical models have been developed to predict the residual strain of reinforced concrete beams during fatigue loading [13-15]. This section briefly describes the analytical model used to estimate the fatigue properties of strengthened RC beam components used in this work.

### 2.1 Fatigue of concrete

Cyclic loading of concrete causes an increase in its strain as the number of cycles increases, i.e. it creates residual strains that resemble creep. The residual strain of concrete in the compression zone under cyclic loading was found to contribute significantly to increases in the deflection of loaded beams [16]. The effects of cyclic residual strain are accounted for using an effective cycle-dependent secant modulus of the elasticity of concrete,  $E_{e,N}$  [17]:

$$E_{e,N} = \frac{\sigma_{\max}}{\varepsilon_{c_{N,\max}}} \quad (1)$$

Where  $N$ = number of cycles,  $\sigma_{\max}$ = the average stress in the concrete at the maximum load level and  $\varepsilon_{c_{N,\max}}$ = total maximum strain at any time. Holmen [18] proposed that the total maximum strain at any time after a given number of cycles is the sum of two components: the elastic strain,  $\varepsilon_{ce}$ , and the evolution of the concrete compressive strain ( $\varepsilon_{c_N}$ ) with the number of loading cycles ( $N$ ), knowing the cyclic creep strain:

$$\varepsilon_{c_{N,\max}} = \varepsilon_{ce} + \varepsilon_{c_N} \quad (2)$$

The evolution of the concrete compressive strain  $\varepsilon_{c_N}$  with the number of loading cycles ( $N$ ) is defined as a function of the mean stress ( $\sigma_c^m$ ), stress range ( $\sigma_c^r$ ), number of cycles ( $N$ ), loading cycle frequency ( $f$ ) and nominal compressive strength of concrete ( $f_c'$ ), as described in Eq. (3) [19]:

$$\varepsilon_{c_N} = 8.417 \times 10^{-6} \cdot \left(\frac{\sigma_c^m}{f_c'}\right) \cdot \left[\left(\frac{N}{f}\right)^{\frac{1}{3}} + 3.87 \cdot \left(\frac{\sigma_c^r}{f_c'}\right) \cdot \left(\frac{N}{9.75}\right)^{\frac{1}{3}}\right] \quad (3)$$

Where the mean stress and the stress range are calculated from the maximum ( $\sigma_{\max}$ ) and minimum ( $\sigma_{\min}$ ) compressive stress applied to the concrete:

$$\sigma_c^m = (\sigma_{\max} + \sigma_{\min})/2 \quad (4)$$

$$\sigma_c^r = (\sigma_{\max} - \sigma_{\min}) \quad (5)$$

Knowing the total maximum strain, the cycle-dependent secant modulus of elasticity for concrete in compression ( $E_{e,N}$ ) after  $N$  fatigue cycles can be computed using Eq.(1). Concrete

under tension is assumed to have no significant tensile strength during cyclic fatigue calculations.

## 2.2 Fatigue of steel

For most civil engineering applications involving reinforced concrete subject to high cyclic fatigue, only the fatigue of the reinforcing steel in the elastic range is taken into account. The elastic fatigue mechanism is responsible for the fracture of the reinforcing steel because the maximum stress during the fatigue life is below the yield point [20]. Fatigue failure of reinforcing steel is caused by microcracking initiated at a stress concentration on the bar surface. The crack gradually propagates as the stress continues to cycle. Sudden fracture occurs when a crack reaches a critical length at which its propagation becomes unstable. The experimental results of Barsom and Rolfe [21] suggest that the modulus of elasticity of the steel remains unchanged until just before the point at which it fails due to high cycle fatigue. It is therefore reasonable to assume that no degradation in residual capacity (strength and stiffness) occurs when reinforcing steel is subjected to service fatigue loading conditions.

## 2.3 Fatigue of CFRP and epoxy

The fatigue performance of FRP composite materials depends on the composition of the matrix and, to some extent, on the type of fiber used [22]. Ferrier et al. [19] found that the decrease in ultimate strength of composite plate can be neglected in the case of carbon/epoxy composites and those cyclic loading causes the stiffness of FRP laminates to degrade according to the following expression:

$$E_{f_N} = m - n \log(N) \quad (6)$$

Where  $E_{f_N}$  is the Young's modulus at cycle (N),  $m$  is the initial Young's modulus, and  $n$  is a constant with a value of 1100. The epoxy between the CFRP laminates and the concrete is assumed to be stiff and not influenced by fatigue loading. This is a reasonable assumption for beams in which failure is initiated in high moment zones, where shear stresses in the epoxy are low [13]. In keeping with this assumption, negligible slippage or debonding between the concrete and CFRP plate was observed before the rupture of the steel bars in the experimental studies presented herein.

## 3. MATERIAL MODELS

The material model used to analyze the behavior of concrete in compression under fatigue loading is that of Warner [23], Figure 1, which accounts for the effect of the concrete's modulus of elasticity in the stress-strain relationship:

$$f = \gamma E + (3 - 2\gamma)E^2 + (\gamma - 2)E^3 \quad (7)$$

Where

$$\begin{aligned} f &= f_c / \bar{f}_c \\ E &= \varepsilon_c / \varepsilon_{cu} \\ \gamma &= E_{e,N} \cdot \varepsilon_{cu} / \bar{f}_c \end{aligned}$$

Here,  $f$  is the normalized concrete stress,  $E$  the normalized strain,  $\gamma$  a dimensionless quantity defining the shape of the concrete's stress-strain relationship,  $E_{e,N}$  the modulus of elasticity of concrete in the  $n$ th load cycle,  $f_c$  the compressive strength of concrete,  $f_c$  the stress in concrete,  $\epsilon_c$  the strain in the concrete, and  $\epsilon_{cu}$  is the ultimate concrete strain. The concrete's strength is taken to be  $0.85 f_c$ ; the factor of 0.85 is included to account for the difference between concrete in a test cube and concrete in a reinforced structure, which stem from differences in geometry, steel reinforcement, load type, rate of loading, and variations in concrete compaction.

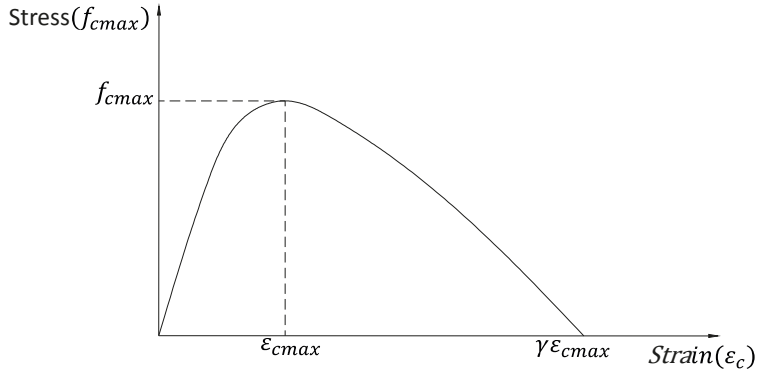


Figure 1- Warner's concrete compression model (1966).

The reinforcing steel is assumed to exhibit linear elastic-perfect plastic behavior; their loading and unloading moduli are both assumed to be equal to its initial elastic modulus. The CFRP material is assumed to exhibit linear brittle failure with the same modulus of elasticity ( $E_{f,N}$ ) during both unloading and reloading.

#### 4. PREDICTING THE FATIGUE OF CFRP-STRENGTHENED REINFORCED BEAMS

The fatigue analyses presented in this paper are based on the lamellar technique in which the cross section of the beam is divided into a series of discrete lamellae or segments (see Figure 2). The fatigue responses of the beams are predicted by calculating the moment-curvature response for the beam under an axial load at equilibrium during each load cycle. The moment-curvature response is obtained by incrementally increasing the beam's curvature and solving for the corresponding value of the applied load. For a given curvature, the moment-curvature response of the cross-section (i.e. the slope of the strain distribution profile) during each load cycle can be obtained by using an iterative process in which the position of the neutral axis for a given strain distribution is adjusted so as to maintain the horizontal force equilibrium within the cross-section of the beam. Assuming that the plane sections remain plane after bending, the location of the neutral axis and the strains in each individual segment are functions of the strain in the topmost segment,  $\epsilon_{top,N}$ , and the curvature,  $\phi$ . The stresses in each segment are calculated from the corresponding strains using the constitutive relationships mentioned earlier. The modulus of elasticity of the concrete and CFRP plate segments are updated in each fatigue cycle. The concrete, CFRP plate, and reinforcing steel within each segment will experience different stresses because each material has a different modulus.

The resultant axial force and the bending moment are obtained by summing the results for all of the segments in the cross-section according to the following equations

$$\sum_{i=1}^m \sigma_i A_i + \text{Tol} = F = 0 \quad (8)$$

$$\sum_{i=1}^m \sigma_i A_i y_i + \text{Tol} = M \quad (9)$$

where  $F$  is the axial load;  $M$  the major bending moment along the beam;  $\sigma_i$  the longitudinal stress at the centroid of fiber  $i$ ;  $A_i$  the area of fiber  $i$ ;  $y_i$  the distance between the centroid of fiber  $i$  and the top of the section;  $m$  the total number of segments in the cross-section, and  $\text{Tol}$  is the maximum tolerable deviation between the calculated force and moment and the externally applied axial load and moment at equilibrium.

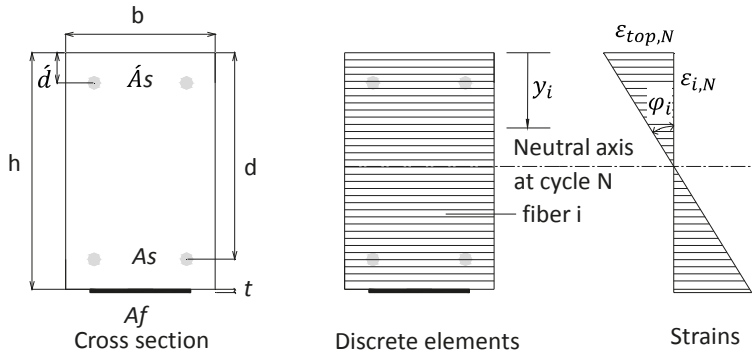


Figure 2- The cross-sectional discretization of a reinforced concrete member strengthened with a CFRP plate.

The moment-curvature calculations for a given load cycle are halted once the number of curvature increments is high enough to resist the maximum applied load.

Once the moment curvature relationship of the cross section has been determined at the end of a load cycle, the load-deflection response of the beam is calculated using a well-known expression from beam bending theory and the flexural stiffness ( $EI$ ) obtained from the slope of the moment-curvature curve (Figure 3)

$$(EI)_N = \frac{\Delta M}{\Delta \phi} \quad (10)$$

Where  $(EI)_N$  is the flexural beam stiffness after  $N$  cycles while  $\Delta M$  and  $\Delta \phi$  are the moment and curvature differences between two load stages during cycle, respectively.

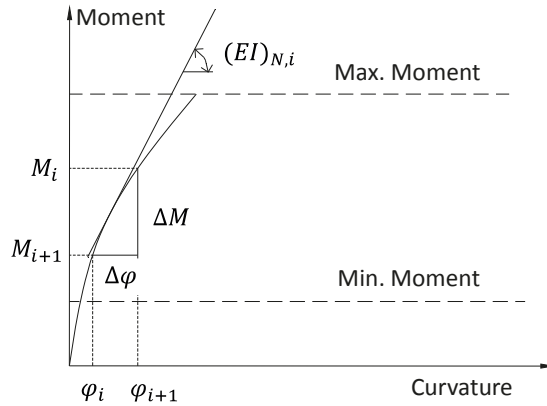


Figure 3- Calculation of flexural stiffness from the moment-curvature relationship.

The main assumptions and limitations of the proposed model are:

1. The strain in each fiber is assumed to be constant over the thickness of a single layer.
2. Negligible contribution of the tensile strength from concrete.
3. Perfect bonding is assumed between concrete and other materials (steel reinforcement and CFRP laminates).
4. The final failure of the structure is governed by the rupture of the first steel reinforcement.
5. Planar sections are assumed to remain planar after bending.
6. The concrete stress-strain behavior implemented in this model represents the behavior of conventional concrete.

## 5. FATIGUE LIFE

A fatigue prediction model should accurately describe the fatigue response of a strengthened beam and also predict the number of cycles to failure. Existing fatigue behavior models are discussed in the previous sections. Since the fatigue life of a CFRP composite is generally greater than that of the reinforcing steel [24], the fatigue life of reinforced concrete beams (whether strengthened or un-strengthened) can be estimated easily using existing steel fatigue life prediction models if the structural members are designed to be under-reinforced [25,26]. Since no delamination occurred before the fatigue fracture of the steel reinforcement, the fatigue life of strengthened beams depends on steel bar rupture. This is assumed to be equal to the life of crack initiation in the steel rebar plus the life during crack growth. In order to produce fatigue life models for strengthened reinforced concrete beams, S-N data for sheets, laminate FRP strengthened beams and NSM-strengthened beams were collected from the literature as shown in Figure 4 [1-4,8,14,27-34]. The figure only includes data for beams that failed by steel bar rupture due to fatigue loading. The stress range ( $S_r$ ) reported is that experienced by the internal reinforcing tension steel during the first cycle. Figure 4 shows a regression curve for strengthened beams obtained using the following equation:

$$S_r = 1038.5 - 132.2 \text{ Log } N_f \quad (11)$$

where  $S_r$  is the stress range of the steel.

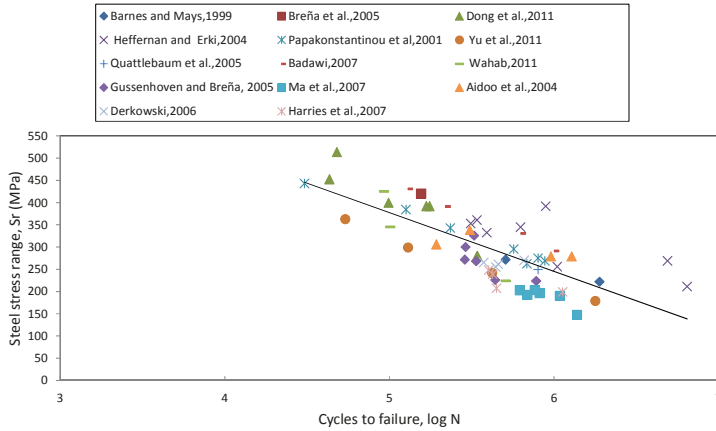


Figure 4- S-N curve for strengthened reinforced concrete beam.

Three established models for estimating the fatigue life of strengthened beams were considered, as shown in Table 1. All three describe the relationship between the reinforcing steel's stress range ( $S_r$ ) and the number of cycles to failure ( $N_f$ ).

Table 1- Fatigue life models

	Fatigue life model
RC beam ,Tilly and Moss [2]	$S_r^9 * N_f = 3.09 * 10^{27}$
RC beam, Model Code [35]	$S_r^5 * N_f = 4.0841 * 10^{17}$
Steel under direct tension in air [36,37]	$\log(N_f) = 6.969 - 0.00555S_r$

## 6. MODEL VERIFICATION

To evaluate the validity of the fatigue model developed in this study, experimental tests were conducted using four CFRP-strengthened RC beams, two strengthened with NSM (Near Surface Mounted) bars and two with traditional plate bonding. One beam of each type was prepared using CFRP with a modulus of elasticity of 200 GPa and the other using CFRP with a modulus of elasticity of 150 GPa. The beams, whose structure is shown in Figure 5, were 300 mm deep, 200 mm wide and had a span length of 3600mm (with a total beam length of 4000mm). Four steel rebars ( $\varnothing = 16$  mm) were used as steel reinforcement (two in the tension and two in the compression region) and stirrups ( $\varnothing = 10$  mm) were installed at a spacing of 75 mm along the beam's span. The average compressive and tensile strengths of the concrete were 71.0 MPa and 4.7 MPa, respectively. The mechanical properties of the steel bars were evaluated in experimental tensile tests. The mean yield strength and modulus of elasticity of the longitudinal steel reinforcement were 578 MPa and 208 GPa, respectively, while those for the stirrups were 533 MPa and 202 GPa, respectively. All of the CFRP strengthening materials were obtained from Sto Scandinavia. The laminates used to strengthen the plate-bonded beams were StoFRP Plate IM (B1-PE1-F; modulus of elasticity = 200 GPa) and StoFRP Plate E (B6-PE2-F; modulus of elasticity = 150 GPa) units, both of which had widths of 143 mm and thicknesses of 1.4 mm. The CFRP bars used to strengthen the NSM bar-strengthened beams were StoFRP BAR IM 10C

(B3-NE1-F; modulus of elasticity = 200 GPa) and StoFRP BAR E 10C (B8-NE2-F; modulus of elasticity = 150 GPa) units. The cross sectional areas of both bar types were 10x10 mm. In the fatigue tests, the specimens were subjected to loads of 6 - 64 kN at a frequency of 1.7 Hz using a four-point loading system.

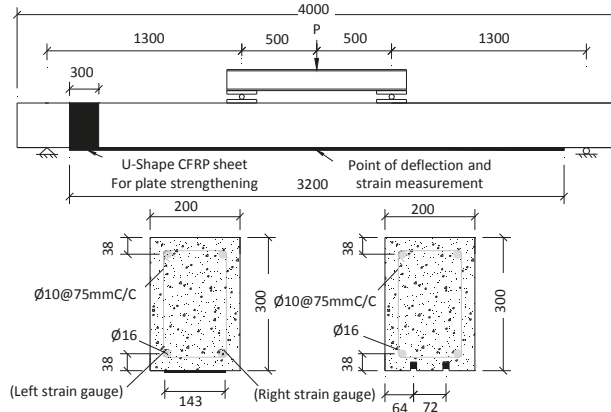


Figure 5- The dimensions of the beam and the four-point loading system used in the experimental studies (top) and cross sections of the plate- and NSM-strengthened reinforced concrete beams (bottom), in [mm].

Figure 6 and Figure 7 shows the deflection of the beam as a function of the number of load cycles for all of the tested specimens and compares these experimental results to the predictions of the new fatigue model. The model's output agrees quite well with the experimental data for all of the beams until the rupture of the first steel rebar. However, the deflections predicted for the beams strengthened with NSM bars seem to be slightly lower than those observed experimentally. This could be because the model assumes that the strengthening CFRP is present as a thin layer covering the underside of the beam rather than in near-surface mounted bars, making the real beams less stiff than would be expected according to the model's assumptions. In addition, the model assumes a perfect bond between the concrete and the carbon fiber reinforcement, which may also contribute to the discrepancy.

Figure 8 and Figure 9 compares the experimental and predicted tensile strains of the internal steel and CFRP. Both strain curves increase rapidly during the initial loading cycles, which are typical for fatigue strain, and then flatten out. The predicted strains are generally in good agreement with the experimental values. As before, the model's predictions deviate relatively strongly from the experimental results for the NSM-strengthened beams because of the failure to account for the effect of the bars' positions.

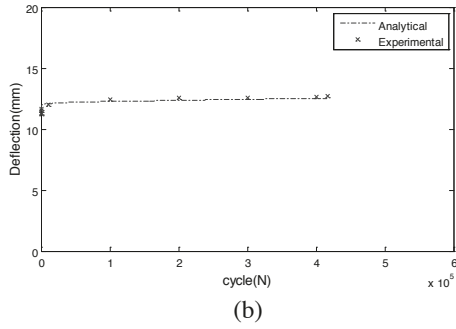
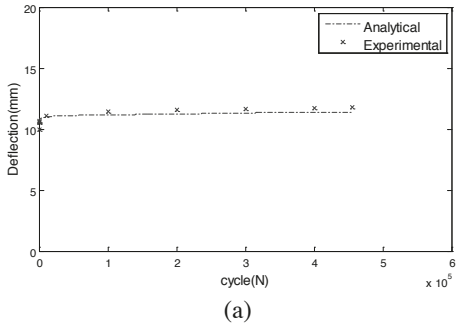


Figure 6- Mid-span deflection as a function of cycle number: (a) Beam B1-PE1-F; (b) Beam B6-PE2-F.

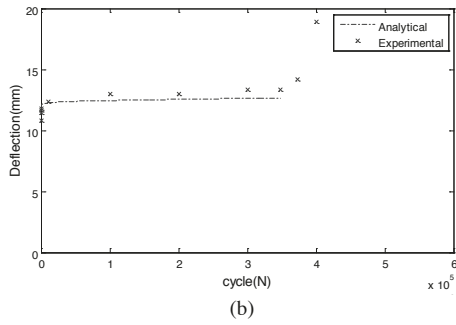
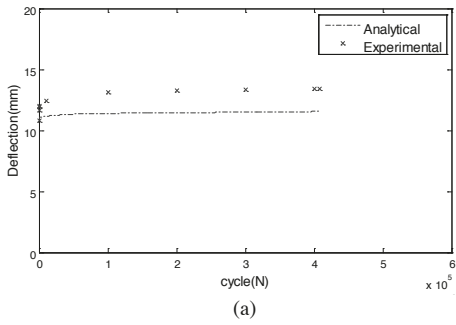
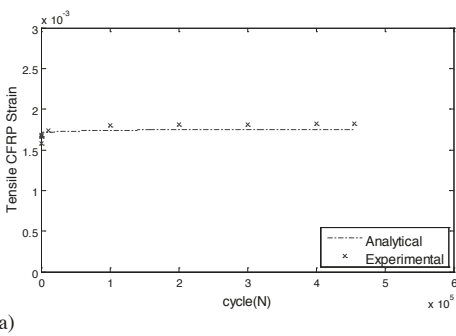
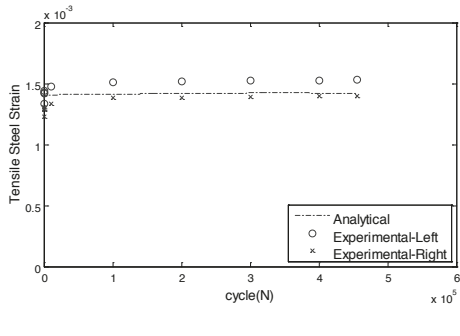


Figure 7- Mid-span deflection as a function of cycle number: (a) Beam B3-NE1-F; (b) Beam B8-NE2-F.



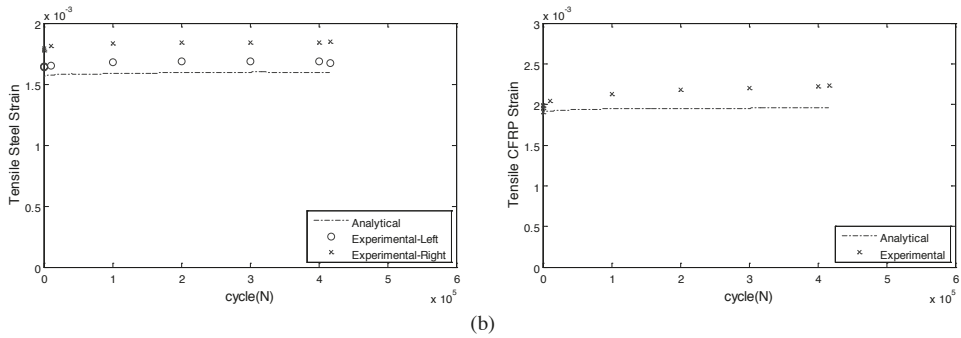


Figure 8-Tensile strains of the mid-span steel reinforcement and CFRP strain as a function of cycle number: (a) B1-PE1-F; (b) B6-PE2-F.

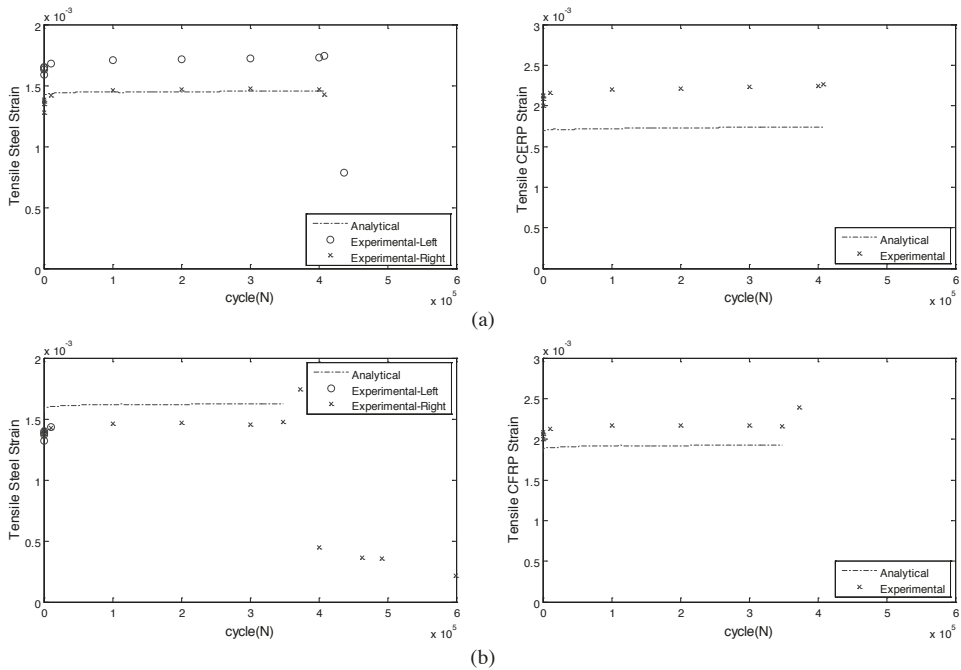


Figure 9- Tensile strains of the mid-span steel reinforcement and CFRP strain as a function of cycle number: (a) B3-NE1-F; (b) B8-NE2-F.

Table 2 lists the number of load cycles prior to steel rupture for each of the tested beams. These experimental results were compared to the predicted fatigue life values generated by the model presented herein and previously reported models, assuming a steel stress range of 258 MPa (see Table 3). The result obtained using the Helgason and Hanson model provides the most conservative estimate of the beam's life, and is in reasonably good agreement with the experimental fatigue life values of the CFRP-strengthened beams. Conversely, the S-N model developed in this work predicts a much longer fatigue life than was achieved experimentally.

This indicates a need to develop an accurate S-N model for strengthened beams under fatigue loads that accounts for the effects of parameters other than the steel stress range such as the presence or absence of shear strengthening, the number of tension steel bars, and the effect of the shear span length.

*Table 2- Fatigue life values for the tested beams.*

Beam	No. of cycles at 1st steel rupture
B1-PE1-F	456,213
B6-PE2-F	416,866
B3-NE1-F	408,094
B8-NE1-F	348,245

*Table 3- Fatigue life values obtained with different S-N models presented in the literature.*

	Estimated fatigue life
Strengthened beam model from this work (Eq.11)	801,555
RC beam model of Tilly and Moss [2]	600,000
RC beam model, Model Code [35]	353,986
Helgason and Hanson model for steel under direct tension in air [37]	342,336

## 7. CONCLUSION

An analytical model has been developed to predict the deflection and residual strain of CFRP-strengthened reinforced concrete beams under fatigue loading. The model is constructed using the lamellar approach and is based on the fatigue properties of the concrete and CFRP strengthening material. Its predictions are in good agreement with the results of experimental studies on CFRP-strengthened beams even though it does not consider the impact of different strengthening methods. Consequently, it cannot describe effects arising from the positioning of NSM bars within soffit beams. However, it can be used to study the evolution of stresses and strains during the fatigue lifetime of a strengthened reinforced beam and it is straightforward to determine the parameters of the model by performing static tests on the individual materials that comprise the beam of interest.

Steel fatigue life models are useful for predicting the number of cycles until failure for strengthened reinforced concrete beams because steel fracture is the primary failure mode in beams strengthened using CFRP. Results presented herein indicate that conservative estimates of a strengthened reinforced beam's fatigue life can be obtained using the Helgason and Hanson equation [37] or the equation presented in the 2010 fib Model Code. The S-N model developed in this work, which were based on experimental data taken from the literature, overestimated the fatigue life of the studied beams. This indicates that there is a need to develop a more accurate S-N model for strengthened beams under fatigue load that accounts for parameters other than just the steel stress range.

## ACKNOWLEDGMENTS

The writers acknowledge the financial support that has been provided by SKANSKA AB, Sto Scandinavia AB, and The Development Fund of the Swedish Construction Industry (SBUF). Also, Lars Åström, Georg Danielsson and Mats Petersson at Testlab, Luleå University of Technology, are acknowledged for their help and support.

## REFERENCES

1. Heffernan P& Erki M., "Fatigue behavior of reinforced concrete beams strengthened with carbon fiber reinforced plastic laminates" *J.Composite Constr.* 2004;8(2),pp.132-40.
2. Barnes RA & Mays GC. "Fatigue performance of concrete beams strengthened with CFRP plates". *J.Composite Constr.* 1999;3(2) .pp.63-72.
3. Aidoo J, Harries KA, Petrou MF. "Fatigue behavior of carbon fiber reinforced polymer-strengthened reinforced concrete bridge girders". *J.Composite Constr.* 2004;8(6) .pp.501-509.
4. Quattlebaum JB, Harries KA, Petrou MF. "Comparison of three flexural retrofit systems under monotonic and fatigue loads". *J.Bridge Eng.* 2005;10(6) .pp.731-40.
5. Johansson U. "Fatigue tests and analysis of reinforced concrete bridge deck models". *Trita-BKN.Bulletin* 2004;76,pp.1-197.
6. Zanuy C, Albajar L, De la Fuente P. "Sectional analysis of concrete structures under fatigue loading". *ACI Struct.J.* 2009;106(5).
7. Mahal M, Blanksvärd T, Täljsten B. "Examination at a Material and Structural Level of the Fatigue Life of Beams Strengthened with Mineral or Epoxy Bonded FRPs: The State of the Art". *Adv.Struct.Eng.* 2013;16(7) .pp.1311-28.
8. Brena SF, Benouaich MA, Kreger ME, Wood SL. "Fatigue tests of reinforced concrete beams strengthened using carbon fiber-reinforced polymer composites". *ACI Struct.J.* 2005;102(2).
9. Al-Hammoud R, Soudki K, Topper TH. "Fatigue flexural behavior of corroded reinforced concrete beams repaired with CFRP sheets". *J.Composite Constr.* 2010;15(1) .pp.42-51.
10. Lin R, Huang P, Zhao C, Guo X, Zheng X. "Prediction of fatigue lives of RC beams strengthened with CFL under random loading". *Acta Mechanica Solida Sinica* 2008;21(4) .pp.359-63.
11. Zheng SS, Wang B, Li L, Zhang L, Hou PJ. "Fatigue-Cumulative Damage Model of RC Crane Girders Strengthened with FRP Strips". *Key Eng Mat* 2008;385,pp.165-8.
12. Yao G, Huang PY, Zhao C. "Flexural fracture and fatigue behavior of RC beams strengthened with CFRP laminates under constant amplitude loading". *Key Eng Mat* 2006;306,pp.1343-8.
13. El-Tawil S, Ogunc C, Okeil A, Shahawy M. "Static and fatigue analyses of RC beams strengthened with CFRP laminates". *J.Composite Constr.* 2001;5(4) .pp.258-67.
14. Papakonstantinou CG, Balaguru PN, Petrou MF. "Analysis of reinforced concrete beams strengthened with composites subjected to fatigue loading". *ACI Special Publication* 2002;206.
15. Oudah F & El-Hacha R. "Analytical fatigue prediction model of RC beams strengthened in flexure using prestressed FRP reinforcement". *Eng.Struct.* 2013;46,pp.173-83.
16. Tan KH & Saha MK. "Glass FRP bonded RC beams under cyclic loading". *International Journal of Concrete structures and materials* 2007;1(1).
17. Balaguru P & Shah S. "A method of predicting crack widths and deflections for fatigue loading". *ACI Special Publication* 1982;75.
18. Holmen JO. "Fatigue of concrete by constant and variable amplitude loading". *ACI Special Publication* 1982;75.
19. Ferrier E, Bigaud D, Clement J, Hamelin P. "Fatigue-loading effect on RC beams strengthened with externally bonded FRP". *Constr.Build.Mater.* 2011;25(2) .pp.539-46.
20. Mogami K, Hayashi T, Ando K, Ogura N. "Elastic-plastic fatigue-crack growth and tearing-instability behavior under cyclic loads". *Int.J.Pressure Vessels Piping* 1990;44(1) .pp.85-97.

21. Barsom JM & Rolfe ST. "Fracture and fatigue control in structures: applications of fracture mechanics". : ASTM International; 1999.
22. Curtis P. "The fatigue behaviour of fibrous composite materials". The Journal of Strain Analysis for Engineering Design 1989;24(4) ,pp.235-44.
23. Warner R & Hulsbos C. "Probable fatigue life of prestressed concrete beams". PCI J. 1966;11(2) ,pp.16-39.
24. Schütz D & Gerharz J. "Fatigue strength of a fibre-reinforced material". Composites 1977;8(4) ,pp.245-50.
25. "Fatigue behaviour of bonded FRP used for flexural retrofit". Proceedings of international symposium on bond behaviour of FRP in structures (BBFS 2005); 2005.
26. Kim YJ &Heffernan PJ. " Fatigue behavior of externally strengthened concrete beams with fiber-reinforced polymers: State of the art". J.Composite Constr. 2008;12(3) ,pp.246-56.
27. Dong Y, Ansari F, Karbhari VM. "Fatigue performance of reinforced concrete beams with externally bonded CFRP reinforcement". Structure and Infrastructure Engineering 2011;7(3) ,pp.229-41.
28. Yu T, Li C, Lei J, Zhang H. "Fatigue of concrete beams strengthened with glass-fiber composite under flexure". J.Composite Constr. 2010;15(4) ,pp.557-64.
29. Badawi MA. "Monotonic and fatigue flexural behaviour of RC beams strengthened with prestressed NSM CFRP rods" 2007.
30. Noran Abdel Wahab. "Bond Behaviour of Beams Reinforced with Near Surface Mounted Carbon Fibre Reinforced Polymer Rods under Fatigue Loading". University of Waterloo; 2011.
31. Gussenhoven R & Brena S. "Fatigue behavior of reinforced concrete beams strengthened with different FRP laminate configurations". ACI Special Publication 2005;230.
32. "Study on fatigue behavior of RC beams strengthened with prestressed CFRP sheets". FRPRCS-8; 2007.
33. Derkowski W. "Fatigue life of reinforced concrete beams under bending strengthened with composite materials". Archives of Civil and Mechanical Engineering 2006;6(4) ,pp.33-47.
34. Harries KA, Aidoo J, Zorn A, Quattlebaum J. "Deterioration of FRP-to-concrete bond under failure loading". Adv.Struct.Eng. 2006;9(6) ,pp.779-89.
35. Comité Euro-International du Béton. " CEB/FIB Model Code 2010". London: Thomas Telford; 2010.
36. Helagson T & Hanson J. "Investigation of design factors affecting fatigue strength of reinforcing bars-statistical analysis". ACI Special Publication 1974;41.
37. Zorn AV. "Effect of adhesive stiffness and CFRP geometry on the behavior of externally bonded CFRP retrofit measures subject to fatigue loads" 2006.

## Development of Engineering Assessment Method for Anchorage in Reinforced Concrete



Mattias Blomfors  
Industrial PhD Candidate  
CBI Swedish Cement & Concrete Research Institute  
Box 857  
SE-501 15 Borås  
Sweden  
E-mail: mattias.blomfors@cbi.se



Kamyab Zandi  
Associate professor  
Chalmers University of Technology



Karin Lundgren  
Professor  
Chalmers University of Technology

### ABSTRACT

There is an increasing need for reliable methods to assess load-carrying capacity and remaining service life of existing infrastructure. Several previous research projects have resulted in a verified, simple 1D model for assessment of anchorage in corroded reinforced concrete structures. Current research aims to extend the 1D model to comprise more practical situations. To verify the 1D model for various cases appearing in practice, such as multiple layers and bundled reinforcement, 3D analyses were carried out. The size of 3D NLFE models required to capture the bond behaviour between corroded reinforcement and concrete is investigated, this to enable efficient analyses. Beam-end models and models of sub-sections with varying sizes and boundary conditions were studied, and the results in terms of bond stress and crack pattern compared. Good agreement was found for several section models; however the choice of boundary conditions largely influence the results and can lead to overestimation of the capacity.

**Key words:** concrete, corrosion, bond, reinforcement, nonlinear FEA

## 1. INTRODUCTION

### 1.1 General

Corrosion of steel reinforcement is the most common cause of deterioration in concrete bridges Bell [1]. Many existing bridges are damaged to varying degrees with corrosion induced cracks or even spalling of concrete cover. The problem with deterioration is also believed to accelerate

in the future due to climate change thus more severe damage can be expected Stewart, Wang & Nguyen [2]. Moreover, the demand on load-carrying capacity of bridges is nevertheless increasing over time. There is therefore a growing need for reliable methods to assess the load-carrying capacity and remaining service-life of existing infrastructure.

Corrosion of reinforcement reduces the cross sectional area of reinforcing bars, and thereby their capacity and ductility. Furthermore, the volume expansion of corrosion products eventually cracks the concrete cover and adversely affects the bond between the reinforcement and concrete; this can result in inadequate anchorage capacity and may cause abrupt failure of the structure. The effect of corrosion on the bond capacity can be modelled using detailed three-dimensional nonlinear finite element (3D NLFE) models, e.g. Coronelli, Zandi & Lundgren [3]. These models are also capable of capturing cracking and spalling of the concrete, but wide practical applications are limited since 3D NLFE analyses require large resources in terms of time and competence.

In order to utilize the knowledge gained from previous research in engineering practice, there is a need for simplified models and tools that are not only accurate enough, but are also time effective for assessment of existing bridges.

## 1.2 Previous work

A simplified 1D model for the Assessment of anchorage in Corroded Reinforced Concrete structures (1D-ARC) has previously been established. It was originally formulated based on the analytical bond-slip model in Model Code 1990 CEB [4] combined with a parametric study using 3D NLFE analyses by Lundgren *et al.* [5]. The model has later been verified using test results of naturally corroded specimens by Perez *et al.*[6], and validated by 3D NLFE analyses and experiments for high corrosion attacks leading to cover spalling in Zandi [7].

The potential of the 1D-ARC model's practical use has been demonstrated in a pilot study of two bridges by Lundgren, Zandi & Nilsson [8]. It was shown that for these two bridges only, the use of the 1D-ARC model reduced the costs by approx. 27 million SEK as unnecessary strengthening could be avoided. This exemplifies that use of this simplified model can result in enormous cost savings for society.

## 1.3 Approach

The previously mentioned case study [8] demonstrated great capabilities of the 1D-ARC model; however, it also revealed question marks for the model to be applied in practice. These question marks include applicability of the model on more realistic scenarios commonly seen in bridges, compared to the ones often used in laboratory test set-ups. For that reason it is aimed to validate or further develop the model for the influence of (i) multilayer reinforcement configuration, (ii) spacing between main bars and stirrups, as well as (iii) bundled and spliced bars.

A parametric study of several cases is to be conducted; therefore it is important to make valid simplifications of the computational model to save modelling and computation time. The focus in this paper is put on choosing the level of detail of the 3D NLFE model needed to capture the bond behaviour in an anchorage region of a beam. In particular, the choice of boundary conditions for the simplified model is investigated.

## 2. STUDIED BEAM GEOMETRY

In order for the assessment tool to be used in practice; it must be applicable to RC beam and slab types commonly seen in bridges. These include several parameters that can vary between structural members, e.g. reinforcement bar diameter, spacing between the reinforcement bars and concrete cover. Furthermore, the reinforcement bars can also be bundled, spliced, and placed in a multilayer configuration. Since corrosion attacks on structures in practice primarily depend on the environmental conditions (location, presence of chlorides etc.), and are not directly associated with the reinforcement layout, the number of situations to be considered in the extension of the 1D-ARC model is large.

The main objective of this paper is to investigate the level of detail required to capture the confining effects from surrounding concrete and stirrups on the bond capacity. Therefore, previously conducted physical tests and detailed 3D NLFE analyses by Zandi, Lundgren & Coronelli [9] of a beam-end were compared to the results obtained from a smaller model of the same geometry.

A beam-end specimen is often used in experimental tests to represent the anchorage region of a beam. It has the shape of an end region of a beam after inclined shear cracking, see Figure 1. A possible source of error for beam-end specimens in general is that the support pressure may increase the confinement around the anchored reinforcement bars and increase the bond capacity. In the test and analyses treated here, the main bars were put in ducts over the supports, i.e. not in contact with the concrete, this to minimize the influence of support pressure and increase the likelihood of anchorage failure.

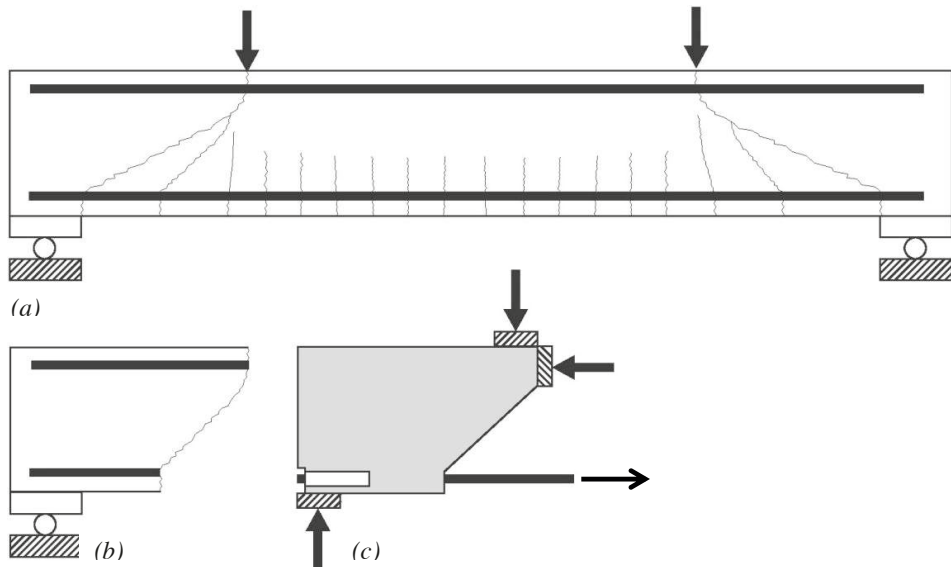


Figure 1: (a) Beam, (b) beam-end specimen and (c) test set-up, adopted from [9].

The studied beam geometry has a square cross-section with 400 mm width and a main bar diameter of 20 mm. One main reinforcing bar is placed in each corner of the cross section with 30 mm concrete cover. An additional bar is placed between the bars in the bottom, giving a total

of three bars to be tested for the anchorage capacity. Load was applied by pulling the bars, and the relative displacement of the reinforcement on both the active and passive side was measured, see Figure 1 c). Two types of specimens which have been subjected to laboratory testing are included in this study: Type A without stirrups and Type B with 8 mm diameter stirrups with 44 mm spacing in the bonded zone. The bonded zone is 210 mm for both beam-end types; see Figure 2.

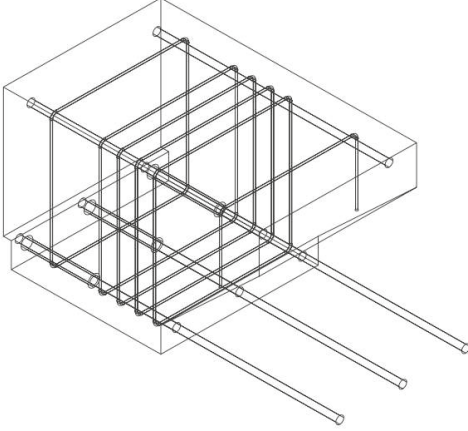


Figure 2: Type B specimen, Type A is similar but without stirrups in the bonded zone

The material parameters for the specimens were tested in [9]. The steel had a yield and ultimate strength of 510 and 610 MPa, respectively, and a Young's modulus of 200 GPa (reinforcement were in elastic range in tests and analyses). The concrete properties, presented in Table 1, vary between the reference and the corroded specimens. This is due to the 3% sodium chloride content in the corroded specimens.

Table 1: Material properties of concrete ( $f_{cc,cyl}$  is the average cylinder 28-day strength,  $f_{ctm}$  is the mean tensile strength,  $G_F$  is fracture energy based on MC 1990,  $E_c$  is elastic modulus based on EC 2)

Specimen	$f_{cc,cyl}$ [MPa]	$f_{ctm}$ [MPa]	$G_F$ [N/m]	$E_c$ [GPa]
Reference	27.7	2.2	61.2	28.7
Corroded	29.7	2.3	64.3	29.4

In the FE analyses, a corrosion level of 1.4% weight loss was applied to all bottom bars for the Type A specimen, while for Type B 1.7% was applied for the corner bars and 0.7% for the middle bar. It should be noted that the corrosion levels were larger for the physical experiments. The damage was however similar, this is explained in more detail in [9].

### 3. NUMERICAL MODELLING OF ANCHORAGE

In this section the bond model for the detailed 3D NLFE analyses is briefly explained. Two types of FE models of different complexity are thereafter presented; one consisting of only a section of the beam and another larger model of the beam-end region. Furthermore, several modelling choices for the smaller model are presented and compared.

### 3.1 Bond model for detailed 3D NLFE analyses

For the detailed analyses using three-dimensional solid elements the bond model is implemented through the use of interface elements between the reinforcement bar and the concrete. The model is capable of describing both the volumetric expansion of a rebar with the associated normal stresses when steel turns into rust, as well as the normal and bond stresses arising when pulling a corroded bar. A detailed presentation of the bond model for detailed 3D NLFE analyses can be found in Lundgren [10-11]. Furthermore the input parameters for the model were chosen as in Jansson *et al.* [12].

### 3.2 Model set-up for detailed NLFE analyses

Two detailed 3D FE models of different sizes were set up in DIANA 9.6 [13] and will be presented in the following sub-sections. The first is a larger model of a beam-end region, while the second model is smaller and includes only a section of the beam. A symmetry condition around the vertical axis is used in both cases, reducing the model size to half.

For both models four node, three-side isoparametric solid tetrahedron elements, approximately 10 mm in size, are used for the concrete and main reinforcement bars. The stirrups are included using embedded elements; this corresponds to full interaction between concrete and stirrups. The entire circumferences of the main bars were corroded; non-uniform corrosion has been investigated in a previous study by Zandi [7] and is excluded in this study.

For concrete, a constitutive model based on nonlinear fracture mechanics using a smeared rotating crack model based on total strain was applied as TNO DIANA [14]. The crack bandwidth, i.e. the distance over which cracks localize, was assumed to be equal to twice the element size. It was later verified by studying the crack localizations in the analyses. The tensile softening of the concrete was modelled according to Hordijk [15] and the compressive behaviour according to Thorenfeldt *et al.* [16]. For the reinforcing steel an isotropic plastic model was used, together with a von Mises yield criterion. The equilibrium iterations were performed using a Quasi-Newton (BFGS) scheme together with a line search algorithm.

#### *Beam-end model*

The beam-end model and boundary conditions are depicted in Figure 3. The load is applied to the bars one at a time, by imposing a deformation on the nodes belonging to the rebar tip. The black triangles represent point supports. The model is fully described in Zandi, Lundgren & Coronelli [9].

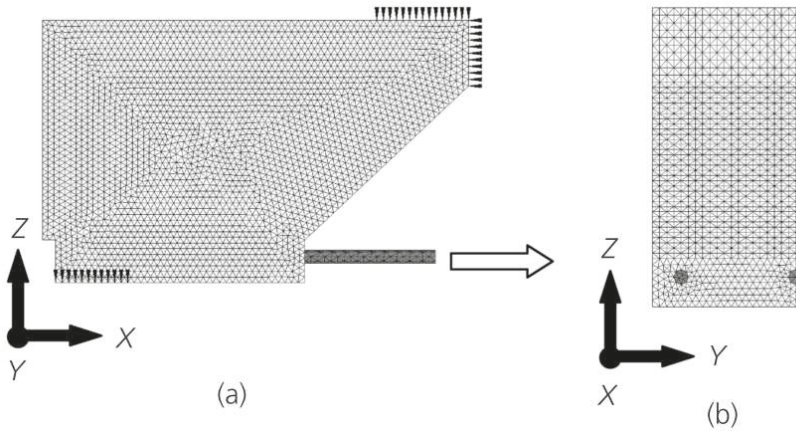


Figure 3: (a) side view, (b) front view of beam-end model

#### Section model

The section models consist of only a part of the beam-end model. The width and height of the section models are 200 mm and 400 mm respectively, same as the beam-end. Four different models are set up, with varying thickness and/or boundary conditions.

The modelled section geometries are 44, 22 and 10 mm thick, this to investigate the influence of section thickness. The first corresponds to one stirrup spacing and if present, the stirrup is located in the centre of the section. The second geometry corresponds to half of the firstly mention, divided at the centreline. Thus half a stirrup is placed at the back of the section. The third section geometry is 10 mm thick, and the stirrup is placed in the centre with a stirrup area per meter of beam chosen equivalent to that of the bonded zone of the test specimen.

For all section models symmetry boundary conditions (BCs) are applied along the centreline of the section and the nodes on the back (opposite side from where the bars are pulled) are fixed in the pulling direction.

Different BCs are chosen on the front of the sections in order to study different alternatives. Two FE models have the same 44 mm thick geometry, but have different sets of BCs on the front. As representation of the compression zone in a beam-end, one has the nodes in the top 90 mm fixed in the pulling direction. This model is named EL44. The other model has all the nodes on the front free to move but forced to remain in the same plane, which resembles a Bernoulli-region in a beam. This model is named EL44-P. In the 22 mm thick section model no conditions are prescribed to the nodes on the front, this in order to study the influence of restraining the front nodes. This model is named EL22. The 10 mm thick model has similar BCs on the front as EL44, i.e. the thought compression zone is restrained against movement in the longitudinal direction. Furthermore, displacement is prevented in the vertical direction in the centre of one of the bars.

The section models EL44, EL44-P, EL22 and EL10 are depicted in Figure 4 (a)-(d).

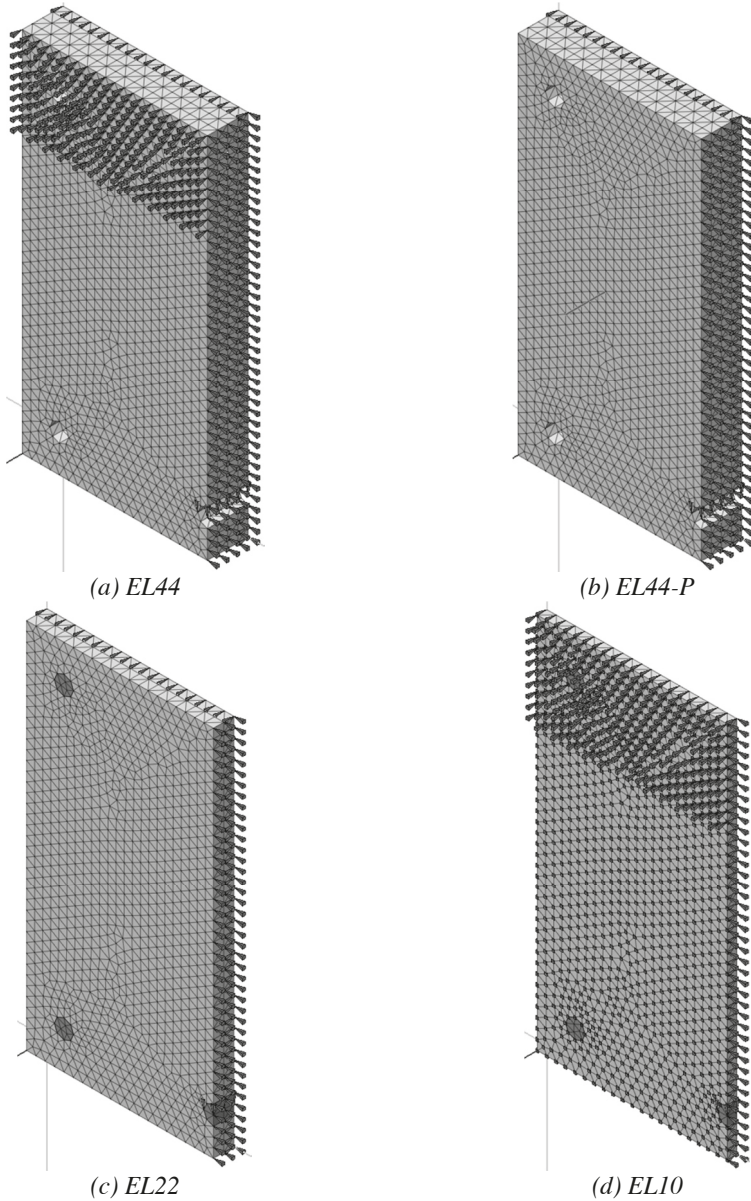


Figure 4: Depictions of section models; (a) EL44: stirrup in centre, (b) EL44-P: stirrup in centre, front nodes restrained to same plane, (c) EL22: half a stirrup in back, (d) EL10: equivalent stirrup in centre. In (a) and (b) the rebar elements are hidden to better see the element size in  $z$ -direction

In the testing procedure the two corner bars were pulled simultaneously, and the middle bar pulled alone. Analogous with the testing procedure and using symmetry conditions, the bars are pulled one by one in the beam-end and section analyses by applying an imposed deformation on

all the end nodes of the pulled bar. The load increment for the section analyses is 0.002 mm/load step.

## **4. RESULTS**

Results from the nonlinear FE analyses of beam sections are presented together with those obtained in previous analyses and tests of beam-end specimens by Zandi, Lundgren & Coronelli [9]. Bond stress curves and crack patterns are presented in the following.

### **4.1 Bond stress curves**

To compare the results from the FE models and tests the average bond stress versus imposed slip of the bar is presented. The average bond stress is for each load step calculated as the reaction force in the pulled nodes divided by the area over which the traction is acting, i.e. the rebar circumference times bonded length.

The results for the Type A and B reference specimens are presented in Figure 5-8 and the corroded cases in Figure 9-11.

Firstly, it is noted that corrosion reduced the maximum average bond stress for all beam-end analyses and tests. For the section analyses the BCs put on the model have a large influence. As a result, the maximum average bond stress could both decrease and increase due to corrosion.

For the Type A reference specimens, see Figure 5 and 6, results in terms of maximum bond stresses from the section models agreed fairly well with test and beam-end values except for EL44-P. This model keeps the front of the section plane, and overestimated the bond capacity for the corner bar. The other three sections showed similar maximum bond capacity, and were in agreement or on the safe side compared to test and beam-end results.

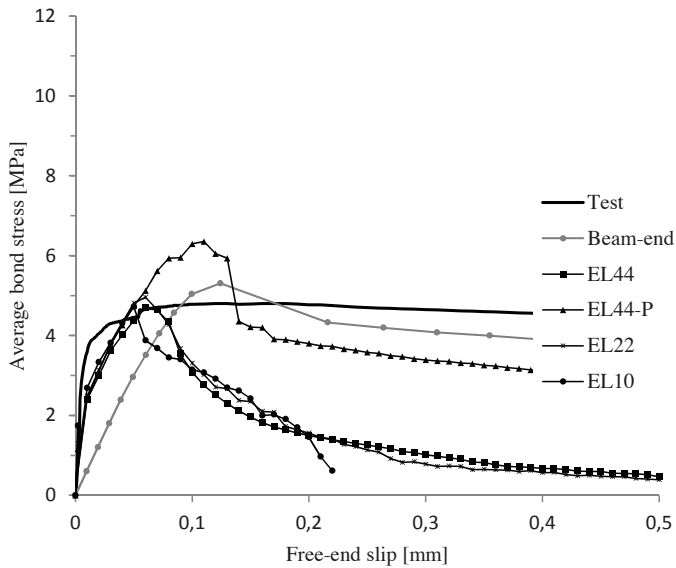


Figure 5: Type A - Reference: corner bar

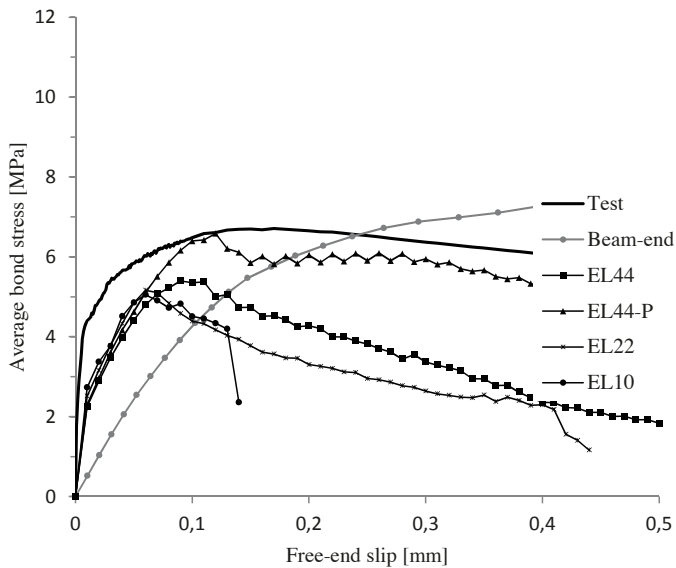


Figure 6: Type A - Reference: middle bar

For the Type B reference specimens, see Figure 7 and 8, the results showed similar patterns as for the Type A specimen. That is, EL10, EL22 and EL44 show similar results, which agree fairly well or are on the safe side compared to tests and beam-end analyses. The EL44-P section

model overestimates the capacity for the corner bar, but agrees well when the middle bar is pulled.

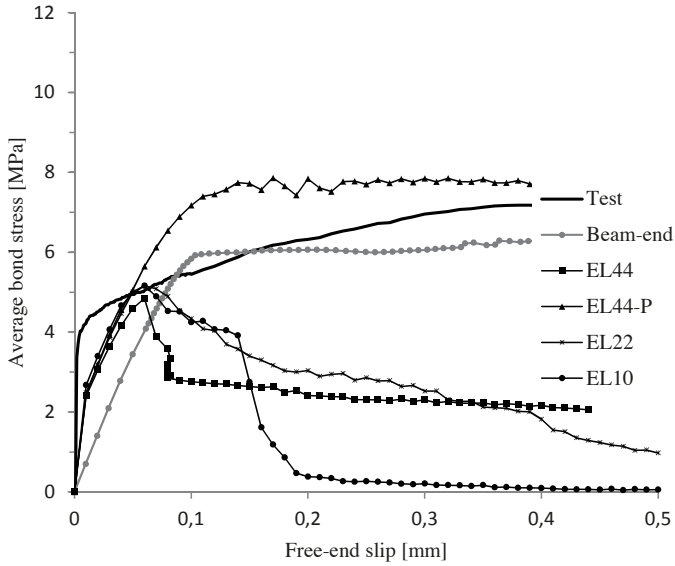


Figure 7: Type B -Reference: corner bar

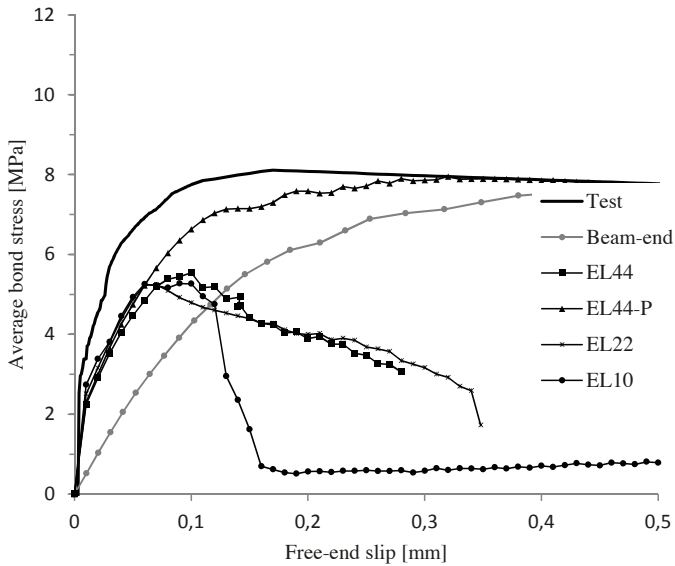


Figure 8: Type B -Reference: middle bar

For the case when 1.4% corrosion was applied to both bars in the Type A specimen (without stirrups), no convergence was obtained for any of the section when pulling the corner bar. This

can be interpreted as if the cover has spalled of the bar, leaving only minor bond capacity. However, when the middle bar was pulled all but EL22 converged. The results are presented in Figure 9.

As previously mentioned, corrosion had an adverse effect on the bond capacity for the test and beam-end model. However, for the section models of the Type B corroded case shows similar or increased capacities. The bond capacity is largely increased for the EL44-P section model, while the other section models show results in line with test and beam-end analyses.

Note that the concrete strength of the reference specimens is slightly lower than for the corroded specimens. However, the beam-end and tests show lower bond capacities if corroded, indicating only small possible influence on the results.

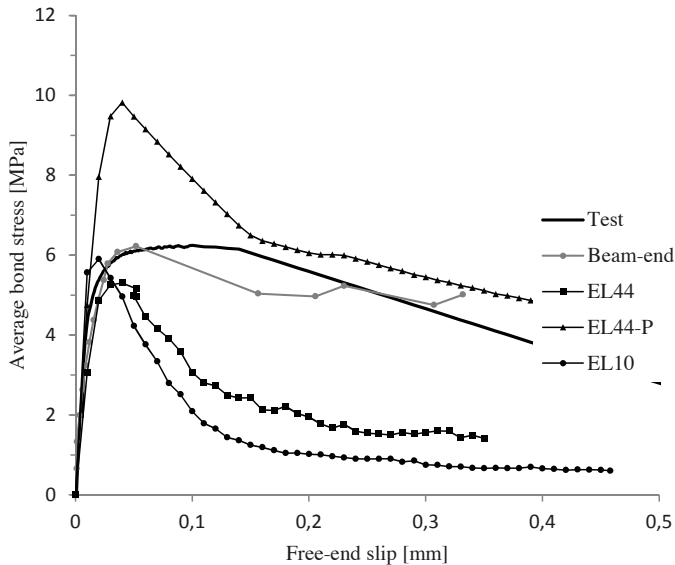


Figure 9: Type A – 1.4% corrosion: middle bar

The results from the corroded Type B specimen are presented in Figure 10 and 11. The beam-end analyses and test values of the bond stress is decreased due to corrosion by around 1-2 MPa. However the EL44-P section model shows an increase in the bond strength of 3 MPa for the middle bar and similar to the reference case for the corner bar. The other three section models produce similar results, which are in agreement with test and beam-end values.

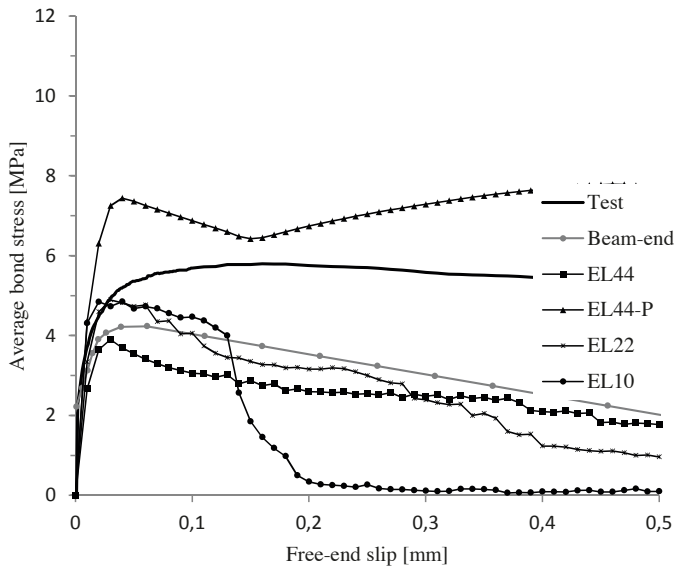


Figure 10: Type B – 1.7% corrosion: corner bar

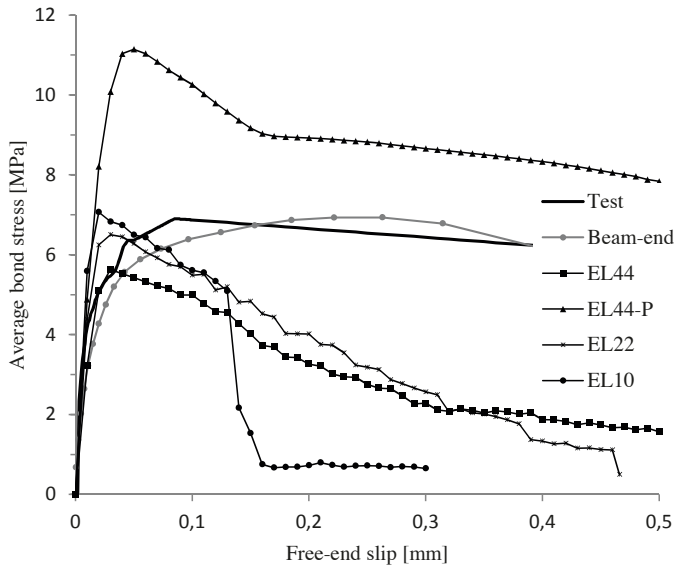


Figure 11: Type B – 0.7% corrosion: middle bar

## 4.2 Crack patterns

Crack patterns obtained at maximum bond stress from the four different section models are presented in this section. The presented results are of the Type B specimen, i.e. with stirrups, with corrosion applied before pulling the bars individually. Red colour indicates a visible crack (1‰ first principal strain), and blue indicates zero strain.

The crack patterns for the two 44 mm thick sections, EL44 and EL44-P, are presented in Figure 12. The crack patterns are similar to those obtained from the beam-end analyses, except for the cracks propagating in the vertical direction. The inclined concrete surface of the beam-end, which thickens the concrete over the height of the specimen, hinders the cracks from propagating upwards. However some vertical cracks, or cracks inclined upwards, are present in the beam-end model. But when present, they are less pronounced in the beam-end model compared to the section model. It should also be noted that the magnitude of the crack widths after the corrosion phase appear to be smaller in the section model compared to the beam-end model for Type B specimens.

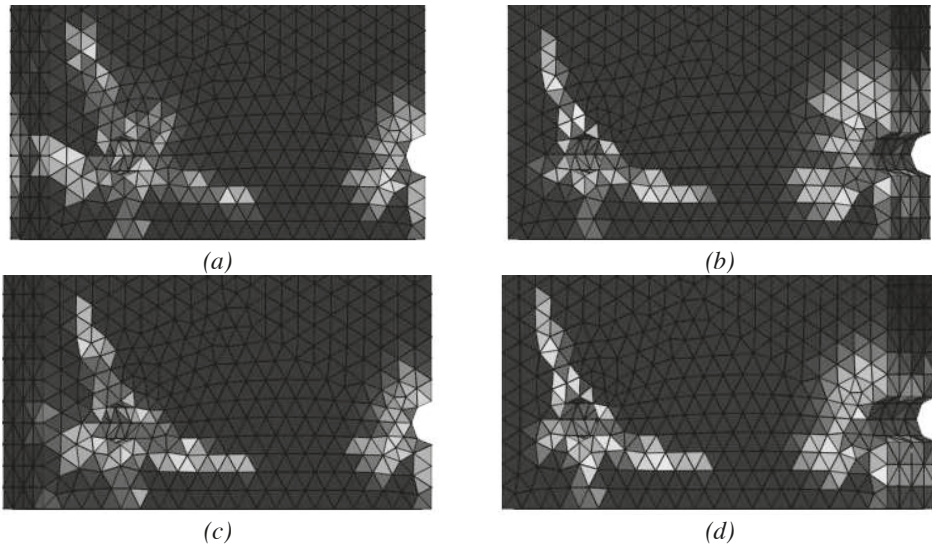


Figure 12: Crack pattern for Type B specimen when subjected to corrosion and bar pull: (a) EL44 - corner bar pulled; (b) EL44 - middle bar pulled; (c) EL44-P - corner bar pulled; EL44-P - middle bar pulled.

The crack patterns for EL22 and EL10 section analyses of the Type B specimen are shown in Figure 13. The 22 mm thick section shows a fairly similar crack pattern compared to the thicker sections, while the 10 mm thick section differs when pulling the corner bar as no crack is propagating downwards. For the 10 mm thick section the horizontal crack to the left is instead more pronounced.

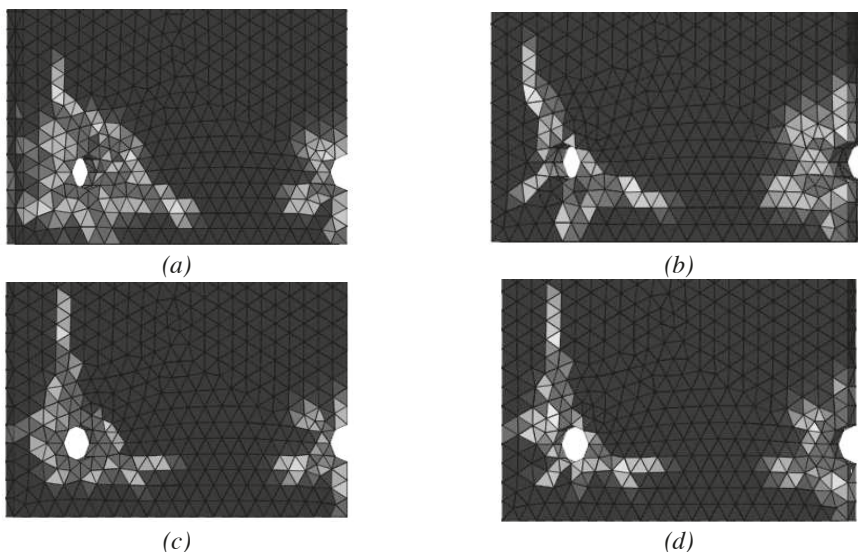


Figure 13: Crack pattern for Type B specimen when subjected to corrosion and bar pull: (a) EL22 - corner bar pulled; (b) EL22 – middle bar pulled; (c) EL10 - corner bar pulled; EL10 - middle bar pulled.

## 5. DISCUSSION

The results in terms of bond capacity agree reasonably well between the section model, the beam-end model and test for most cases. However, the EL44-P section model where the front was forced to remain plane, showed higher capacity than the beam-end and test values in several cases. The stresses around the pulled bar were studied, and this BC gave rise to compressive stresses around the bar. This is a possible explanation for the difference in bond capacity, since the section models with other BCs showed tensile stresses in the pulling direction around the pulled bar.

The other models EL44, EL22 and EL10 gave fairly similar results, which were corresponding to, or on the safe side, compared to beam-end analyses and tests. However there was a tendency of the thickest model to give slightly lower bond capacity in the case of corrosion than the thinner models. It was checked that the thickness still was small enough to ensure local slip response, so a lower average stress cannot be attributed to varying slip levels along the embedment length. This indicates that the corrosion induced stresses affect the bond of a thicker model more, compared to a thinner model.

The bond stiffness is similar for all section models, and corresponds well to both beam-end and test for the corroded cases. However, for the reference cases all FE analyses give a weaker response than the physical tests. This is due to the calibration of the bond model, which is aimed at capturing the maximum capacity rather than the behaviour at small slip levels. Furthermore, in the representation of the physical test results the free end slip was used. This also contributes to the difference in stiffness compared to the section analyses, where the displacements were obtained from the active end (front of section).

No difference in the bond capacity could be observed between the section models with concrete nodes restrained in the compressions zone (EL44 and EL10) compared to a completely unrestrained concrete front surface (EL22). By studying the stresses it was seen that the restraint at the top 90 mm did not influence the stresses at the bar level, thus the results are reasonable.

An adequate section model simplifies and speeds up the advanced analyses required for the extension of the 1D-ARC model. Furthermore, a section model could also be used to study cases that are particularly hard to model. For instance, a beam-end model with several layers of reinforcement experiences a large anchoring force and is prone to develop an unintended crack at the end of the anchorage length as the tensile capacity of the concrete is exceeded. This study has shown the importance of the boundary conditions when moving from a larger to a smaller model. Furthermore, it will also be investigated if a section model can be used for modelling a region of a beam with spliced reinforcement, a case of large practical interest.

## **5.1 Conclusions and outlook**

The following conclusions regarding bond capacity can be stated based on comparison of results from section analyses, beam-end analyses and experiments:

- 1) For all considered cases the boundary conditions put on the section model have large influence on the results;
- 2) Restraining the concrete surface around the bars on the front of the section can cause compressive stresses and lead to excessive capacity;
- 3) Without corrosion, the capacity were similar or on the safe side for several of the section models;
- 4) With corrosion, the capacity agreed well for several of the section models, but the section model with concrete restrained around the pulled bars showed too high capacity;
- 5) The crack patterns were similar in the section and beam-end analyses, as well as in the experiments.

In future work physical, statistical and model uncertainties of the basic variables will be incorporated in the 1D-ARC model. The probabilistic 1D-ARC model will be set up using suitable distribution functions as inputs of the basic variables. Such a model will enable reliability evaluation of different structural elements and also probabilistic service-life prediction. Furthermore, it can also be used to quantify modification factors for the deterministic resistance model, which enables deterministic service-life prediction.

## REFERENCES

- [1] Bell B. "Sustainable Bridges D1.3 European Railway Bridge Problems". 2004. Available from [www.sustainablebridges.net](http://www.sustainablebridges.net)
- [2] Stewart M.G., Wang X., Nguyen, M.N. Climate change impact and risks of concrete infrastructure deterioration. *Eng Struct.* 2011; **33**(4): 1326-1337.
- [3] Coronelli D., Zandi Hanjari K., Lundgren K. Severely Corroded RC with Cover Cracking. *J Struct Engineering-ASCE.* 2013; **139**(2): 221-232.
- [4] CEB. CEB-FIP model code 1990. *Bulletin d'Information 213/214 CEB.* 1993.
- [5] Lundgren K., Kettil P., Zandi Hanjari K., Schlune H., Soto San Roman A. Analytical model for the bond-slip behaviour of corroded ribbed reinforcement. *Struct Infrastruct E.* 2012; **8**(12): 157-169.
- [6] Perez I., Tahershamsi M., Marí A.R., *et al.* 1D and 3D analysis of anchorage in naturally corroded specimens. Paper presented at: *Proceedings of the 10th fib International PhD symposium in Civil Engineering; 2014 Jul 21-23; Quebec, Canada.* 2014. p. 547-552.
- [7] Zandi K. Corrosion-induced spalling and anchorage capacity. *Struct Infrastruct E.* 2015; **11**(12): 1547-1564.
- [8] Lundgren K., Zandi Hanjari K., Nilsson U. A model for the anchorage of corroded reinforcement: validation and application. Paper presented at: *fib Symposium, Concrete - Innovation and Design; 2015 May 18-20; Copenhagen, Denmark.* 2015. p. 1-11.
- [9] Zandi Hanjari K., Lundgren K., Coronelli D. Bond capacity of severely corroded bars with corroded stirrups. *Mag Concrete Res.* 2011; **63**(11): 953-968.
- [10] Lundgren K. Bond between ribbed bars and concrete. Part 1: Modified model. *Mag Concrete Res.* 2005; **57**(7): 371-382.
- [11] Lundgren K. Bond between ribbed bars and concrete. Part 2: The effect of corrosion. *Mag Concrete Res.* 2005; **57**(7): 383-395.
- [12] Jansson A., Lofgren I., Lundgren K., Gylltoft K. Bond of reinforcement in self-compacting steel-fibre-reinforced concrete. *Mag Concrete Res.* 2012; **64**(7): 617-630.
- [13] TNO DIANA. FEM-software - release 9.6. Delft, The Netherlands. 2015.
- [14] TNO DIANA. DIANA finite element analysis user's manual - release 9.6. Delft, The Netherlands. 2015.
- [15] Hordijk D.A. Local approach to fatigue of concrete. PhD thesis, Delft University of Technology. Delft, The Netherlands. 1991.
- [16] Thorenfeldt E., Tomaszewicz A., Jensen J.J. Mechanical properties of high-strength concrete and applications in design. Paper presented at: *Conference on Utilization of High-strength Concrete; Stavanger, Norway.* 1987. p. 149-159.

## Research Council and Editorial Board for Nordic Concrete Research

Dr. Marianne Tange Hasholt, Chairman for the Research Council

<b>Danish Concrete Association</b>	Dr. Marianne Tange Hasholt Associate professor Technical University of Denmark Department of Civil Engineering Mobile: <a href="mailto:matah@byg.dtu.dk">matah@byg.dtu.dk</a>	Mrs. Gitte Normann Munch-Petersen Teknologisk Institut Kongsvang Allé 29 DK - 8000 Aarhus Mobil +45 72 20 32 45 <a href="mailto:gnmp@teknologisk.dk">gnmp@teknologisk.dk</a>
<b>Finnish Concrete Association</b>	Professor Jouni Punkki Aalto University, Dept of Civil Engineering P.O.Box 12100 FI-00076 Aalto, Finland tel. +358 50 322 4155 <a href="mailto:jouni.punkki@aalto.fi">jouni.punkki@aalto.fi</a>	Prof. Dr. Jukka Lahdensivu Tampere University of Technology P.O.Box 527 FI-33101 Tampere Mobile: +358 40 0733852 <a href="mailto:jukka.lahdensivu@tut.fi">jukka.lahdensivu@tut.fi</a>
<b>Icelandic Concrete Association</b>	Dr. Jón E. Wallevik Innovation Center Iceland IS - 112 Keldnaholti Tel: +354 522 9362 Mobile: +354 Fax: +354 522 9111 <a href="mailto:jon.w@nmi.is">jon.w@nmi.is</a>	Prof. Dr. Olafur H. Wallevik Innovation Center Iceland IS - 112 Keldnaholti Tel: +354 522 9000 Mobile: +354 <a href="mailto:wallevik@ru.is">wallevik@ru.is</a>
<b>Norwegian Concrete Association</b>	Dr. Terje F. Rønning Heidelberg Cement NE / Cement Product development & Implementation P.O.Box 38 N - 3991 Brevik Tel.: +47 3557 2000 Mobile: +47 915 76 046 <a href="mailto:terje.ronning@heidelbergcement.com">terje.ronning@heidelbergcement.com</a>	Prof. Dr. Mette R. Geiker Department of Engineering NTNU N - 7034 Trondheim Tel: +47 7359 4529 Mobile: +47 4045 1218 <a href="mailto:mette.geiker@ntnu.no">mette.geiker@ntnu.no</a>
<b>Swedish Concrete Association</b>	Tekn. Dr. Peter Utgenannt CBI Swedish Cement and Concrete Research Institute P.O. Box 857 SE - 501 15 Borås Tel: +46 105 166 870 Mobile: +46 706 452 008 <a href="mailto:Peter.utgenannt@cbi.se">Peter.utgenannt@cbi.se</a>	

December 6<sup>th</sup> 2016





ISBN: 978-82-8208-052-1 ISSN: 0800-6377  
Printed by Helli - Visuell kommunikasjon, Oslo